minerals

MDPI

Article

Stable Isotope (S, Mg, B) Constraints on the Origin of the Early Precambrian Zhaoanzhuang Serpentine-Magnetite Deposit, Southern North China Craton

Jie Meng [1,2,3,*], Houmin Li [2], Yanhe Li [2], Zhaochong Zhang [3], Lixing Li [2] and Zhe Song [2,4]

1 Development and Research Center of China Geological Survey, Beijing 100037, China
2 MNR Key Laboratory of Metallogeny and Mineral Assessment, Institute of Mineral Resources, Chinese Academy of Geological Sciences, Beijing 100037, China; lihoumin2002@163.com (H.L.); lyh@mx.cei.gov.cn (Y.L.); llixing@cags.ac.cn (L.L.); ddsz.2007@163.com (Z.S.)
3 State Key Laboratory of Geological Processes and Mineral Resources, Faculty of Earth Sciences and Resources, China University of Geosciences, Beijing 100083, China; zczhang@cugb.edu.cn
4 Faculty of Earth Resources, China University of Geosciences, Wuhan 430074, China
* Correspondence: mengjie12@mails.ucas.ac.cn; Tel.: +86-1058-584-343

Received: 23 May 2019; Accepted: 18 June 2019; Published: 22 June 2019

Abstract: The origin of the Zhaoanzhuang serpentine-magnetite deposit in the southern North China Craton (NCC) is highly disputed, with some investigators having proposed an ultramafic origin, whereas others favor a chemical sedimentary origin. These discrepancies are largely due to the difficulty in determining the protolithic characteristics of the highly metamorphosed rocks. Sulfur, magnesium, and boron isotope geochemistry combined with detailed petrography was carried out in this study to constrain the original composition of the Zhaoanzhuang iron orebodies. Anhydrite is present as coarse crystals intergrown with magnetite, indicating that the anhydrite formed simultaneously with the magnetite during metamorphism rather than as a product of later hydrothermal alteration. The anhydrite has a narrow range of positive $\delta^{34}S$ values from +19.8 to +22.5‰ with a mean value of +21.1‰. These values are significantly higher than that of typical magmatic sulfur ($\delta^{34}S$ = 0 ± 5‰) and deviate away from primary igneous anhydrite towards mantle-sulfur isotopic values, but they are similar to those of marine evaporitic anhydrite and gypsum (~+21‰). The sulfur isotopic compositions of several samples show obvious signs of mass-independent sulfur fractionation ($\Delta^{33}S$ = −0.47‰ to +0.90‰), suggesting that they were influenced by an external sulfur source through a photochemical reaction at low oxygen concentrations, which is consistent with the Neoarchean-Paleoproterozoic atmosphere. Coarse-grained tourmaline from the tourmaline-rich interlayers of the orebodies occurs closely with Mg-rich minerals such as phlogopite, talc, and diopside, indicating that it has a metamorphic origin. The $\delta^{11}B$ values of the tourmaline range from −0.2‰ to +3.6‰ with a mean value of +2.0‰, which is much positive relative to that of magmatic tourmaline but is consistent with that of carbonate-derived tourmaline. The magnesium isotopic analyses of the serpentine–magnetite ores and the magnesium-rich wall rocks revealed a wide range of very negative $\delta^{26}Mg$ values from −1.20‰ to −0.34‰ with an average value of −0.80‰. The value is higher than that of ultramafic rocks ($\delta^{26}Mg$ = −0.25‰) and exhibits minor Mg isotopic fractionation. However, these values are consistent with those of marine carbonate rocks, which have lower $\delta^{26}Mg$ values and larger Mg isotopic variations ($\delta^{26}Mg$ = −0.45‰ to −4.5‰). Collectively, the S–Mg–B isotopic characteristics of the Zhaoanzhuang iron orebodies clearly indicate a chemical sedimentary origin. The protoliths of these orebodies most likely reflect a series of Fe–Si–Mg-rich marine carbonate rocks with a considerable evaporite component, indicating a carbonate-rich superior-type banded iron formation precipitated in an evaporitic shallow marine sedimentary environment.

Keywords: serpentine–magnetite ores; southern North China Craton; sulfur isotopes; magnesium isotopes; boron isotopes; superior-type BIF

1. Introduction

The Zhaoanzhuang iron deposit in the southern North China Craton (Figure 1) consists of abundant uncommon serpentine–magnetite ores, with an ore reserve more than 130 Mt (≥40% Fe). The ore is composed of low-Ti magnetite (TiO_2 ~0.1%), high-Mg serpentine ($Mg^{\#}$ = 92.42–96.55), and minor amounts of dolomite, apatite, anhydrite, and gypsum [1]. The high-Mg serpentine in the ore is believed to be the retrograde metamorphic product of high-Mg olivine (Fo = 89–90) and orthopyroxene (En = 89–90) [1], which is supported by the presence of minor amounts of residual olivine and orthopyroxene. The magnetite-poor wall rocks adjacent to the ores characteristically contain various magnesium-rich silicate minerals, including olivine (Fo = 83–87), orthopyroxene (En = 82–86), hornblende (X_{Mg} = 0.87–0.96), and humite ($Mg^{\#}$ = 82–84), which coexist with lesser amounts of anhydrite, dolomite, and apatite [1]. In addition, several layers of tourmaline-rich rock are interlayered with the iron ores and the magnetite-poor wall rocks.

Early researchers ascribed the formation of the serpentine–magnetite ores to magmatic processes, and regarded the magnetite, apatite, and magnesium-rich silicate minerals as ultramafic proxies [2–15]. However, the common occurrence of dolomite and anhydrite intergrown with serpentine and magnetite and the low-Ti nature of magnetite are inconsistent with a magmatic origin [1]. In addition, olivine could also be formed by metamorphism of Fe–Mg-rich carbonate rocks [16]. Thus, it could be a metamorphic mineral that occurs with the humite, tremolite, and spinel in highly metamorphosed siliceous carbonate rocks [17,18], or a metasomatic mineral in carbonate-related magnesian skarn rocks that produced by contact metasomatism [19,20]. Thus, the magnesium-rich silicate minerals (olivine, orthopyroxene, hornblende, and humite) in the iron ores and wall rocks of the Zhaoanzhuang iron deposit could also have a metamorphic or metasomatic origin and be derived from a carbonate-rich protolith.

Stable isotopes are important to understand the protolithic characteristics of high-grade metamorphic rocks, because isotopic fractionation is often limited in high-temperature metamorphic processes [21,22]. In iron orebodies, large abundances of anhydrite and gypsum that coexist with magnetite, magnesium-rich silicates in the ores and wall rocks, and locally enriched interlayered tourmaline-rich rocks can be used to investigate the sulfur (S), magnesium (Mg), and boron (B) isotopic compositions.

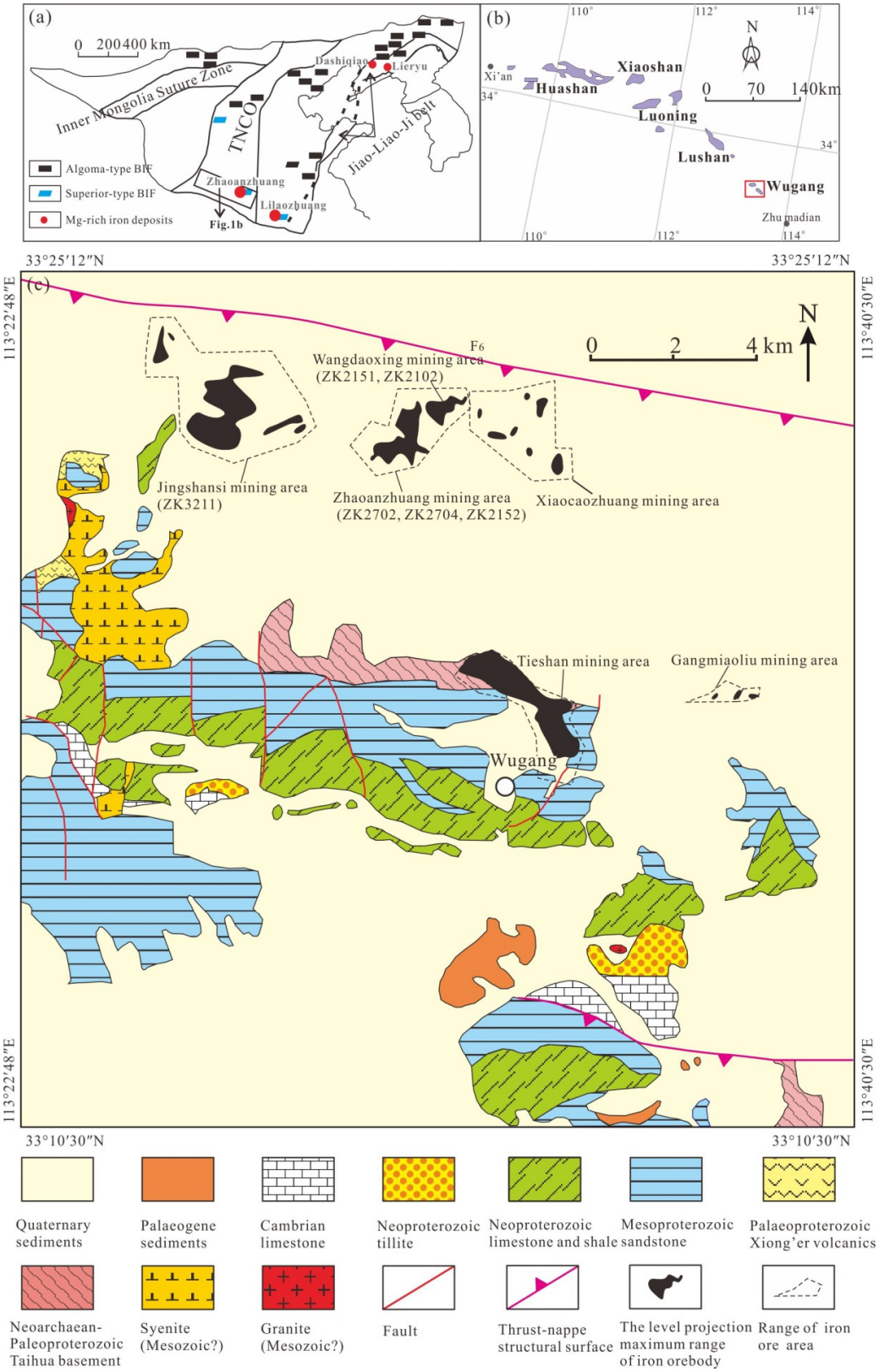

Figure 1. (**a**) Schematic tectonic map of the North China Craton, showing the locations of the Precambrian iron deposits (after [23–25]). (**b**) Map of the Early Precambrian metamorphic terranes in the southern part of the North China Craton. (**c**) Geologic map of the iron deposits in the Wugang terrane, Henan (modified from [1,26–28]).

Previous studies have shown that the S isotopic composition of metamorphic rocks is closely related to that of their protoliths [29,30]. The isotopic behavior of sulfur in magmatic and sedimentary processes varies significantly. The isotopic fractionation of S during melting in the upper mantle is insensitive, and the magmatic sulfur isotopic composition ($\delta^{34}S$) approaches that of meteoritic sulfur (0 ± 3‰) [31–33]. Thus, ultramafic-mafic rocks from the upper mantle generally have meteoritic sulfur isotopic compositions [31,34,35]. Granitic magmas have high positive $\delta^{34}S$ values when they are contaminated by marine sedimentary sulfur [30]. In terrestrial geological processes (near-surface non-biotic and biotic oxidation-reduction, weathering, and evaporation), sulfur is redox-sensitive and vulnerable to fractionation, resulting in thermodynamic nonequilibrium, kinetic isotopic effects, and a broad range of $\delta^{34}S$ values that deviate significantly from zero [31,34].

Studies have also shown that the seawater throughout geologic time has had a very positive $\delta^{34}S$ value, resulting in seawater-derived sulfate minerals that are strongly enriched in ^{34}S [31,34,36]. In addition, as a traditional theoretical phenomenon, mass-dependent sulfur isotopic fractionation occurs in thermodynamic equilibrium reactions and kinetic non-equilibrium reactions [37–39]. However, in some cases, significant mass-independent sulfur isotopic fractionation occurs ($\Delta^{33}S = \delta^{33}S - 1000 \times [(1 + \delta^{34}S/1000)^{0.515} - 1] \neq 0$). This feature is thought to result from photochemical reactions of SO_2 in an anoxic atmosphere and has been observed in older sulfide and sulfate minerals throughout the geologic record [39–44]. Samples that have inherited the effects of mass-independent sulfur isotopic fractionation that occurred in the geologic past have undergone an exogenic sulfur cycle [44–46]. Therefore, S isotopic fractionation can be used to discriminate magmatic, terrestrial, and marine depositional processes as well as the superposition of these processes.

For Mg isotopes, numerous rigorous isotopic geochemical studies have shown that Mg isotopes can be used as an effective indicator to distinguish magnesium sources for metamorphosed sedimentary and igneous rocks [47,48]. Mg isotopic fractionation is very sensitive to low-temperature processes, such as Mg–calcite, dolomite, and magnesite precipitation, continental and chemical silicate weathering, and biological processes [48–58]. However, it is limited during partial melting, crystal fractionation, and low- to high-temperature metamorphic processes [47,59–66]. Igneous rocks, ranging from peridotite to granite, and magmatic minerals (olivine, orthopyroxene, clinopyroxene, and hornblende) generally have identical chondritic Mg isotopic compositions (average $\delta^{26}Mg = -0.25 \pm 0.07$‰) [47,59–62,67–69].

During chemical weathering, the lighter Mg isotopes in the silicate rocks are more likely to migrate into the hydrosphere, while the heavier Mg isotopes are left behind [54,65]. As a result, the clastic and saprolite sediments in the continental crust produced by various levels of low-temperature chemical weathering and sedimentation often have a wide range of $\delta^{26}Mg$ values that tend towards heavier Mg isotopic compositions [54], while the Mg isotopes of rivers have variable values with average $\delta^{26}Mg = -1.09$% [51,65] and the Mg isotopic composition of seawater is homogeneously light ($\delta^{26}Mg = -0.8 \pm 0.1$‰) due to the relatively long residence time of Mg in the oceans [54]. Relative to seawater, marine sediments, and carbonates often have a wider range of lighter Mg isotope ($\delta^{26}Mg$) values (–5.57‰ to −1.09‰) [51,70,71] due to the weak Mg bond strength in carbonate minerals [72,73]. In addition, the effect of the Mg/(Mg + Ca) ratio on concentration during carbonate precipitation may also play an important role in controlling Mg isotopic fractionation [58], which is supported by the fact that dolomite has the highest ^{26}Mg of all of the carbonate minerals [58].

Since boron is enriched in the continental crust, seawater, and arc volcanics [74], all of which display widely varying isotopic compositions, the B isotopic compositions of the major natural boron reservoirs, including volcanic rocks, marine and non-marine evaporates, clastic and pelitic sediments, and a variety of fluids, are relatively well characterized [74–80]. In general, magmatic sources typically have negative $\delta^{11}B$ values, whereas positive $\delta^{11}B$ values indicate a marine contribution [76,81].

Without changing electrovalence, B isotopes are insensitive to redox conditions. However, as a highly mobile element, B can be significantly fractionated during various geologic processes, such as precipitation of sediment from seawater and diagenesis, as well as various interactions between hydrothermal fluids, meteoric water, and B-bearing minerals [78,81,82]. During fluid–solid

precipitation, diagenesis, and dehydration metamorphism, the heavier B isotopes are preferentially retained by the fluid while the lighter B isotopes are incorporated into B-bearing minerals, such as tourmaline [77,83,84]. As a result, tourmaline $\delta^{11}B$ values generally represent minimum compositions for the source reservoirs [77]. In addition, as the most abundant boronsilicate mineral in natural rocks [85], tourmaline is a potential indicator of provenance due to its refractory nature and is highly resistant to post-ore hydrothermal alteration and metamorphism [77,86–89]. In magmatic rocks, the tourmaline $\delta^{11}B$ values are likely to approximate the $\delta^{11}B$ of the source rocks due to its highly incompatible nature, which results in it being easily partitioned into the melt phase and limits isotopic fractionation during magmatic differentiation and postmagmatic water–rock interaction [90]. However, tourmaline associated with marine evaporate- or carbonate-derived B sources has a wide range of positive $\delta^{11}B$ values [77]. Therefore, B isotopic composition is a reliable indicator of tourmaline's original sources.

In this study, we present results of a comprehensive study involving petrography and S–Mg–B isotope geochemistry to constrain the material provenance and formation environment of the serpentine–magnetite ores of the Zhaoanzhuang iron deposit. The results and conclusions also shed light on the effectiveness of using S–Mg–B isotopes as protolith indicators for high-grade metamorphic rocks.

2. Regional Setting

The North China Craton (NCC) is the oldest and largest craton in China [23], where various types of large-scale ore deposits were formed during the Early Precambrian, including Archean-Paleoproterozoic banded iron formations (BIFs), Paleoproterozoic Cu–Pb–Zn and strata-bound magnesite and boron deposits, and Mesoproterozoic REE–Fe–Pb–Zn deposits [91].

Tectonically, the NCC is believed to have formed by amalgamation of the Eastern and Western Blocks of the trans-North China Craton (TNCO, Figure 1a) at ~1.85 Ga [92,93]. In addition, two orogenic belts were formed in the Eastern and Western Blocks (Figure 1a). The Eastern Block underwent a Paleoproterozoic rifting event, which formed the Longgang and Langrim Blocks, followed by the collision of these two blocks at ~1.9 Ga, which formed the N-S striking Jiao-Liao-Ji Belt [94]. The Western Block was subdivided into the Yinshan Block in the north and the Ordos Block in the south. These blocks are now separated by the E-W trending Khondalite Belt, which formed at ~1.95 Ga due to the collision of the two blocks [94].

The Taihua Group outcrops in several terranes (the Huashan, Xiaoshan, Luoning, Lushan, and Wugang terranes) throughout the southern part of the TNCO (Figure 1a,b). Based on differences in lithology, structure, metamorphism, and age, the Taihua Group is subdivided into two distinct lithotectonic units [95], the Lower Taihua Group and the Upper Taihua Group. The Lower Taihua Group mainly consists of tonalitic–trondhjemitic–granodioritic (TTG) gneisses, which formed during the Neoarchean-Early Paleoproterozoic (ca. 2.8–2.4 Ga) [95–100], and also contains amphibolite and minor granitic plutons and mafic dikes. The Upper Taihua Group formed during the Paleoproterozoic (ca. 2.3–1.84 Ga) [95,98,99], which unconformably overlies the Lower Taihua Group and is composed of Khondalite-dominated supracrustal rocks, including metapelitic gneisses, marbles, quartzites, and banded iron formations (BIFs), as well as minor amounts of mafic granulites, amphibolites, and granitoids [95,101]. Several studies have revealed that the Taihua Group experienced high-grade upper amphibolite–granulite facies metamorphism [13,95,98,102] from 1.97 to 1.80 Ga ([103] and reference therein).

In the eastern terrane of the southern TNCO (Figure 1b), the Neoarchaean-Paleoproterozoic crystalline basement is unconformably overlain by the unmetamorphosed volcanic rocks of the Xiong'er Group (1.80–1.77 Ga) [104,105], Mesoproterozoic sandstones, Neoproterozoic limestone, tillite, and shale, Cambrian limestone, and Paleogene and Quaternary sediments (Figure 1c). The magmatic rocks (Mesozoic granite and syenite) are locally exposed in the study area (Figure 1c) [10]. The Taihua Group, as the oldest metamorphic basement exposed in this terrane, is traditionally

subdivided into the Zhaoanzhuang, Tieshanmiao, and Yangshuwan formations from the bottom to the top. The Zhaoanzhuang Formation is mainly composed of amphibolites and marbles; the Tieshanmiao Formation is mainly composed of TTG gneisses, amphibolites, marbles, and banded iron formations; and the Yangshuwan Formation is predominantly composed of metapelitic gneisses. The Zhaoanzhuang serpentine–magnetite deposit is hosted in the Zhaoanzhuang Formation. The amphibolites and metapelites in this terrane recorded the 1.96 to 1.92 Ga tectonothermal event and its associated upper amphibolite–granulite facies metamorphism [13,102,106].

3. Geology of the Ore Deposit

The iron deposits in the Wugang region include the Jingshansi, Zhaoanzhuang, Xiaocaozhuang, Tieshan, and Gangmiaoliu mining areas (Figure 1c). The Jingshansi, Tieshan, and Gangmiaoliu iron deposits are Tieshanmiao-type deposits [28], while the Zhaoanzhuang and Xiaocaozhuang iron deposits are Zhaoanzhuang-type deposits. Extensive descriptions of the geology of the Zhaoanzhuang ore deposit have been made by previous studies [2,6,7,12,14,15,26,27,107].

3.1. Strata

The strata distributed in the Zhaoanzhuang area, which have been exposed by drilling, mainly include the Zhaoanzhuang formation and minor amounts of Mesoproterozoic sandstone as well as Eogene and Quaternary sediments (Figure 2). The lithologic units of the Zhaoanzhuang formation can be divided into six members from the bottom to the top: (1) A lower iron ore-bearing section mainly consisting of diopside–hornblende–oligoclase gneiss and oligoclase–hornblende gneiss, which are intercalated with two segments of serpentine–magnetite ores; (2) almandine–oligoclase–hornblende gneiss member; (3) an oligoclase–hornblende gneiss member; (4) the main orebody; (5) a diopside–oligoclase gneiss member; and (6) a banded granitic migmatite member (Figure 2) [10,108].

The lower iron ore-bearing member is not exposed in the drill hole No. ZK2702 (Figure 2). In the drill hole No. ZK2704, only the corresponding third hornblende–oligoclase gneiss and fourth iron ore-bearing lithologic sections occur. Thus, the iron mineralization is poorly developed in the drill hole No. ZK2704, but a tourmaline-rich rock layer is present. In addition, two layers of tourmaline-rich rock were discovered in the drill hole No. ZK2151 (not shown in Figure 2).

The iron orebodies occur as laminar to lenticular structures, parallel to the upper and lower lithologic sections, with a maximum length of 1840 m, width of 530 m, and depth of 82 m (after Wuyang Mining Limited Liability Company, Henan Ansteel Group) within the diopside–hornblende–oligoclase gneiss. The accumulative iron reserves of these orebodies are 89 Mt with an average Fe grade of 36.67 wt.%.

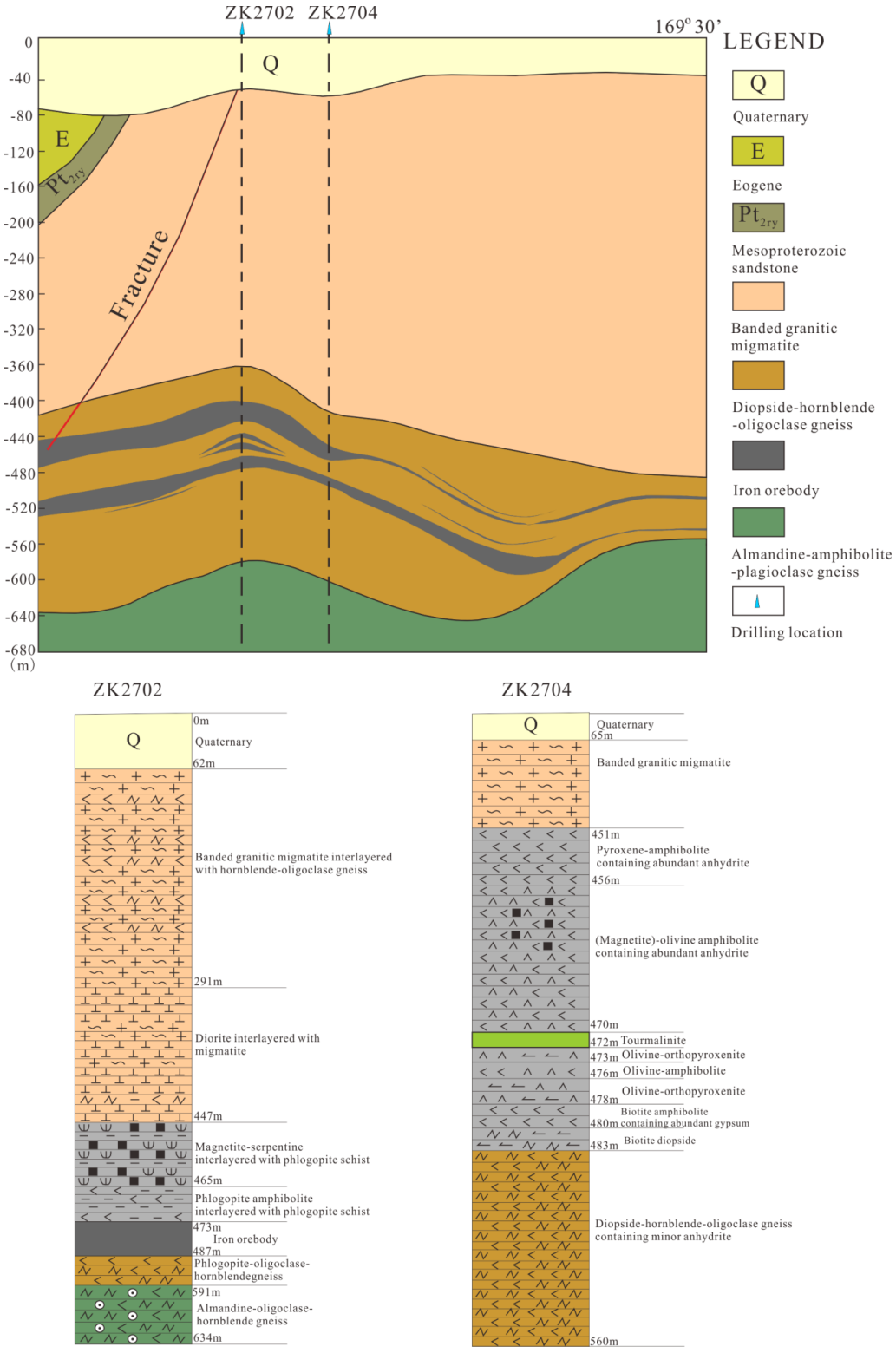

Figure 2. Geologic map of the Zhaoanzhuang area, showing the locations of drill holes ZK2702 and ZK2704 (after Wuyang Mining Limited Liability Company, Henan Ansteel Group). Stratigraphic columns for drill holes ZK2702 and ZK2704 are also shown.

3.2. Mineralogy and Paragenesis

The Zhaoanzhuang iron deposit is characterized by distinct and complex mineral components, including magnetite, serpentine, olivine, orthopyroxene, hornblende, clinohumite, spinel, apatite,

dolomite, anhydrite, gypsum, phlogopite, and tourmaline with trace amounts of Mg-rich ilmenite, talc, muscovite, monazite, thorite, and xenotime (after Wuyang Mining Limited Liability Company, Henan Ansteel Group). In this study, electron microscopy (EMS) and energy disperse spectroscopy (EDS) were used to make the petrographic observations.

3.2.1. Ore and Wallrock Types

Based on the components of gangue minerals, the iron ore types include serpentine–magnetite ores (Figure 3a–c), apatite–magnetite ores (Figure 3d), carbonate–magnetite ores (Figure 3g–i), and hornblende–magnetite ores with banded, disseminated, and dense disseminated textures (Figure 3). The serpentine is most likely a retrograde magnesium-rich silicate mineral, because minor relict olivine and orthopyroxene are observed in the iron ores (Figure 3a). Drilling surveys show that serpentine–magnetite ores are dominant, followed by apatite- and carbonate-magnetite ores, while hornblende-magnetite ores are the least common. Our observations reveal that transitional ore types are common, including apatite–serpentine–magnetite (Figure 3c), serpentine–carbonate–magnetite (Figure 3h,i), and apatite–carbonate–magnetite ores. In addition, a considerable amount of anhydrite is present in the various types of iron ores (Figure 3c,h), and anhydrite–magnetite ores are even present (Figure 3e,f). The anhydrite gradually grades to gypsum from the edge to the interior of the mineral (Figure 3f).

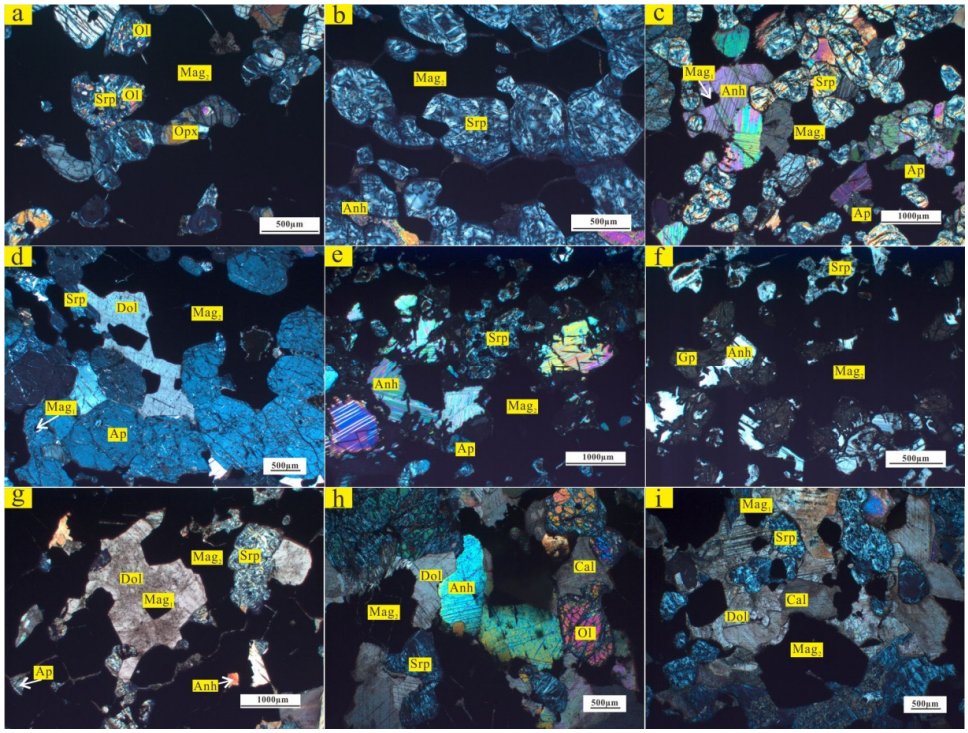

Figure 3. The mineral assemblages of the different types of iron ores in the Zhaoanzhuang iron deposit. (**a**) Dense disseminated serpentine–magnetite ore with residual olivine and orthopyroxene. (**b**) Banded serpentine–magnetite ore with minor anhydrite. (**c**) Disseminated serpentine–magnetite ore with abundant anhydrite and minor apatite. (**d**) Apatite–magnetite ore with irregular dolomite and minor serpentine. (**e**) Anhydrite–magnetite ore with serpentine and minor apatite. (**f**) Anhydrite–magnetite ore with serpentine. (**g**) Carbonate–magnetite ore with serpentine, apatite, and anhydrite. (**h**) Carbonate–magnetite ore containing magnetite, olivine, serpentine, anhydrite, dolomite, and calcite. The dolomite exhibits planar boundaries in contact with anhydrite, but curved boundaries in contact with magnetite and serpentine. (**i**) Carbonate–magnetite ore with serpentine. Abbreviations: Anh, anhydrite; Ap, apatite; Cal, calcite; Dol, dolomite; Gp, gypsum; Mag, magnetite; Ol, olivine; Opx, orthopyroxene; Srp, serpentine. All the photos were taken in cross-polarized light.

The wall rocks adjacent to the iron ores mainly include olivine–orthopyroxenite (Figure 4c,d,f), olivine–(orthopyroxene)–amphibolite (Figure 4e,g–i) and interlayered serpentinized olivine–marble (Figure 4a,b). In addition, there are various thinly layered tourmaline-rich rocks (Figure 5a–c); anhydrite–, calcite–, and phlogopite–(apatite)–serpentinite (Figure 5d,e,g); and anhydrite–phlogopite schist (Figure 5f,h,i) in the interlayers of the wall rocks.

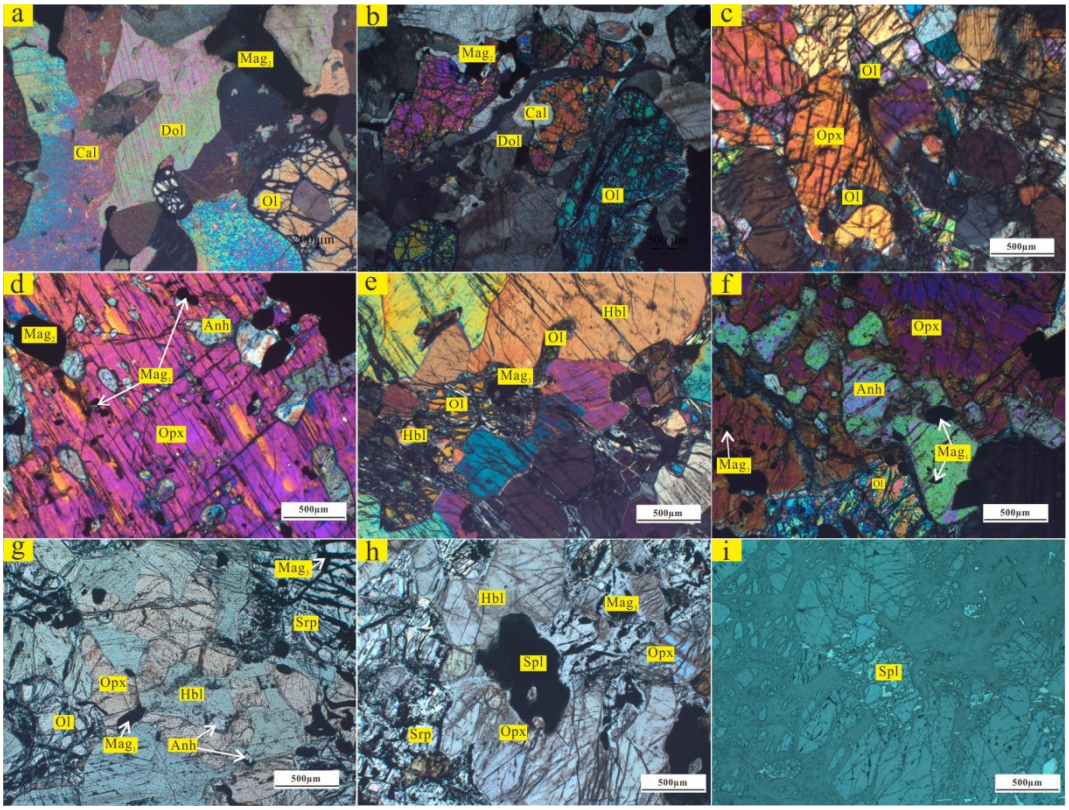

Figure 4. The mineral assemblages of the different types of wall rocks in the Zhaoanzhuang iron deposit. (**a**) Olivine–dolomitic marble with magnetite. (**b**) Olivine–dolomitic marble with magnetite. (**c**) Olivine–orthopyroxenite. (**d**) Tabular orthopyroxene contains abundant anhydrite and minor magnetite (Mag_1) inclusions. (**e**) Olivine–amphibolite. (**f**) Olivine–orthopyroxenite with residual anhydrite. (**g**) Olivine–orthopyroxene-amphibolite. (**h**,**i**) Olivine–amphibolite containing orthopyroxene and spinel. Abbreviations: Anh, anhydrite; Cal, calcite; Dol, dolomite; Hbl, hornblende; Mag, magnetite; Ol, olivine; Opx, orthopyroxene; Spl, spinel; Srp, serpentine. (**a–f**) photos were taken in cross-polarized light. (**g**,**h**) Photos were taken in plane-polarized light. (**i**) Photo was taken in reflected light.

3.2.2. Paragenetic Sequence of the Ore and Gangue Minerals

Magnetite is the dominant ore mineral. Based on mineral associations and textural relationships, the Zhaoanzhuang iron deposit appears to have experienced at least three stages of mineralization. Figure 6 shows the paragenetic relationships and sequence of the main mineral assemblages. The magnetite does not contain ilmenite exsolutions, but it does occur alongside minor amounts of granular magnesium-rich ilmenite or iron magnesia spinel, indicating co-genetic mineral phases. Based on its various occurrences and paragenetic minerals, the magnetite develops in three distinct stages. The first prograde metamorphic stage generated thin magnetite (Mag_1) within anhydrite, apatite, dolomite, and orthopyroxene (Figure 3c,d,g,i; Figure 4d,f,g). The second-peak metamorphic stage generated coarse-grained magnetite (Mag_2) as well as olivine, orthopyroxene, hornblende, serpentine, dolomite, apatite, and anhydrite. The third retrograde metamorphic stage generated dotted and fibrous magnetite (Mag_3) within serpentine (Figure 4e,g,h).

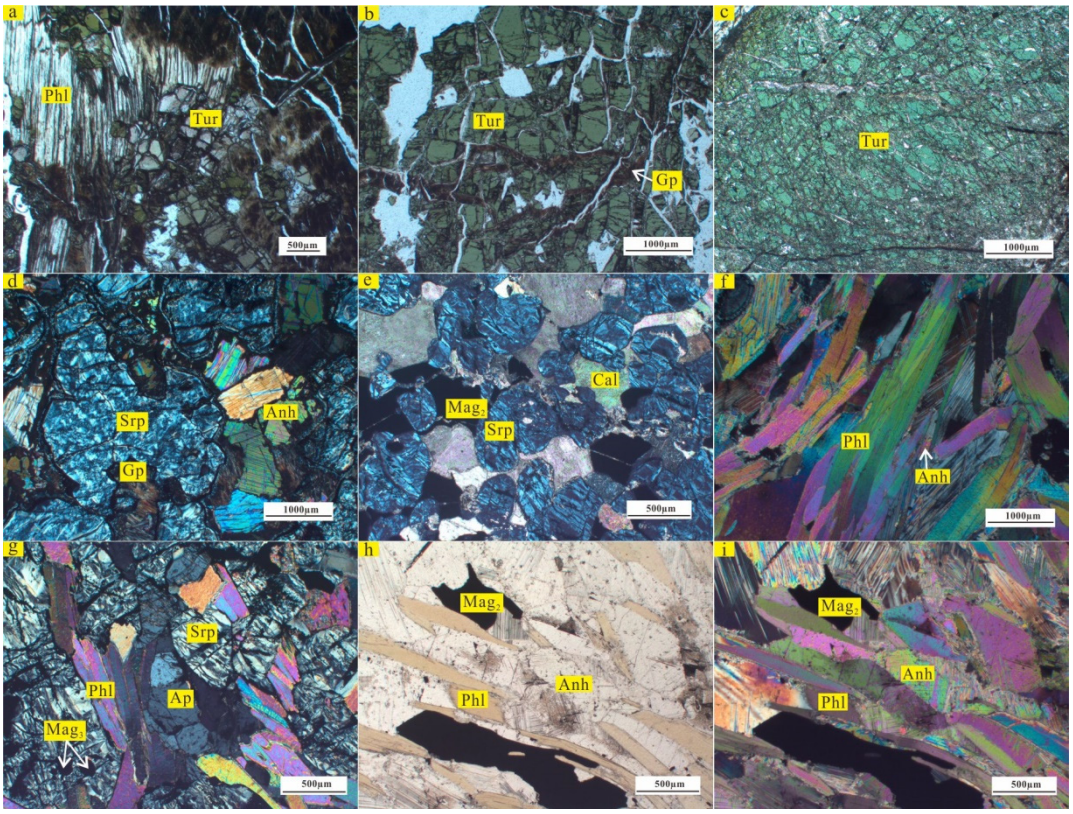

Figure 5. The mineral assemblages of other typical wall rocks in the Zhaoanzhuang iron deposit. (**a–c**) Tourmaline-rich rocks. (**d**) Anhydrite–serpentinite. (**e**) Calcite–serpentinite with some magnetite. (**f**) Anhydrite–phlogopite schist. (**g**) Apatite–phlogopite–serpentinite. (**h**) Anhydrite–phlogopite schist with minor magnetite. Abbreviations: Anh, anhydrite; Ap, apatite; Cal, calcite; Gp, gypsum; Mag, magnetite; Phl, phlogopite; Srp, serpentine; Tur, tourmaline. (**a–c**,**h**) Photos were taken in plane-polarized light. (**d–g**,**i**) Photos were taken in cross-polarized light.

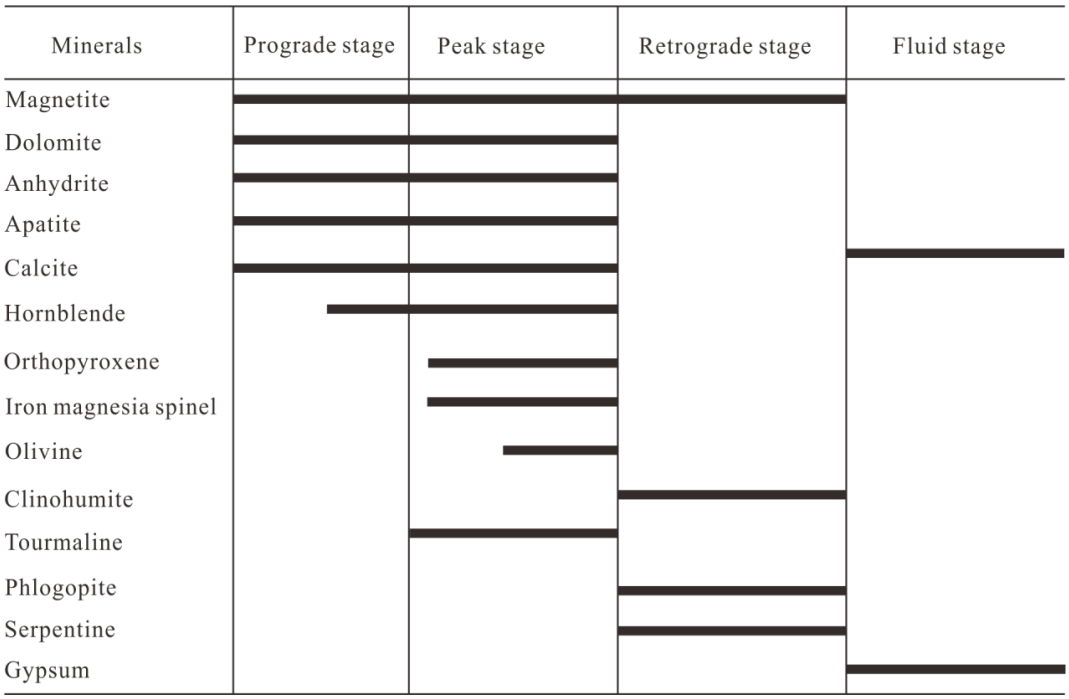

Figure 6. Paragenetic sequence of the minerals in the Zhaoanzhuang iron deposits in different metamorphic stages.

The wall rocks contained minerals similar to the gangue minerals in the iron ores, but the minerals in the wall rocks were coarser than those in the ores (Figure 4). Subhedral to anhedral olivine and orthopyroxene were present in the dolomitic marble (Figure 4a,b) that is interlayered within the iron orebody. These minerals were most likely derived from a metamorphosed Mg-rich dolomite since the dolomite grain boundaries exhibit an embayed structure (Figure 4a,b). Mg-poor calcite is often observed within the Mg-rich olivine or interstitially between the curved Mg-rich dolomite and subhedral olivine (Figure 4a,b). These features are most likely to represent metamorphic reaction textures [$2CaMg(CO_3)_2 + SiO_2 = 2CaCO_3 + Mg_2SiO_4 + 2CO_2$]. In addition, anhydrite coexisting with dolomite, olivine, and minor magnetite was also observed throughout the dolomitic marble. Similarly, dolomite and anhydrite with irregular forms and curved grain boundaries were commonly observed in the carbonate– and (serpentine)–apatite–magnetite ores (Figure 3d,g–i). In serpentine–magnetite ores, anhydrite and minor apatite coexists with serpentine and magnetite (Figure 3c,e,h). The dolomite, anhydrite, and minor amounts of magnetite, calcite, and apatite are, thus, earlier than the magnesium-rich silicates. However, the magnesium-rich silicates in the wall rocks and iron ores could be associated with the Mg-rich siliceous carbonates.

The wall rocks close to the ores mainly consist of Mg-rich olivine, orthopyroxene, hornblende (primarily tremolite), and several other Mg-rich minerals such as clinohumite, spinel, and ilmenite. In some of the wall rocks, fine-grained anhydrite coexisting with minor magnetite is disseminated within the coarse-grained tabular orthopyroxene (Figure 4d,f). The olivine formed later than the hornblende and orthopyroxene, because the olivine grains are located in the interstitial spaces between the hornblende and orthopyroxene grains (Figure 4c,e–h). In addition, the orthopyroxene is thought to have formed later than the hornblende because the fine-grained irregular orthopyroxene and iron magnesia spinel simultaneously grew along the boundaries of the hornblende grains (Figure 4g–i), suggesting that the coexisting orthopyroxene and spinel associations are the result of the decomposition of hornblende. Clinohumite is an F-rich magnesium-rich silicate with various grain sizes and textures. It occurs around the orthopyroxene and olivine grains or as individual minerals in the olivine–orthopyroxene or olivine–amphibolite rocks, indicating its late-stage formation.

In the iron orebodies, considerable hydrous minerals, such as tourmaline, serpentine, and phlogopite are developed (Figure 5). The tourmaline, which is coarser grained and enriched in some of the rocks (Figure 5a–c), coexists with phlogopite (Figure 5a), diopside, and talc and is cut by gypsum veins (Figure 5b). This suggests that the tourmaline is a metamorphic mineral of this ore-forming system, rather than a late stage exotic mineral. Serpentine occurs with abundant anhydrite, calcite, and phlogopite, and there are minor amounts of magnetite and apatite in the serpentinite (Figure 5d,e,g). The serpentine did not contain much leaching magnetite, suggesting that it has a low Fe content. In the phlogopite-rich rocks, phlogopite occurs along an orientation intergrown with minor parallel rains of anhydrite and magnetite (Figure 5f,h,i). Other minor minerals include biotite, muscovite, talc, and rare REE-rich monazite, thorite, and xenotime, which are hosted in the apatite. Sulfides are relatively rare. Only a few pyrite crystals were found surrounding the magnetite.

4. Sample Descriptions and Analytical Methods

4.1. Sample Descriptions

Thirty-five samples of anhydrite and gypsum intergrown with magnetite and serpentine were collected from the Zhaoanzhuang iron deposit. Gypsum is a late hydration product of anhydrite, so the analytical samples are actually a mixture of them. The mineralogic compositions of all of the samples were analyzed using X-ray diffraction (XRD) at the Institute of Mineral Resources, Chinese Academy of Geological Sciences (CAGS). The analytical results are shown in Table 1 and Table S1. Because the anhydrite is an earlier mineral that intergrown with dolomite, it should be approximately representative of the original materials. Owing to the scarce occurrence of the sulfides and other

sulfur-bearing minerals, the S isotope compositions of anhydrite and gypsum could be used to assess the sulfur isotopic fractionation characteristics of the past geological environment.

Table 1. S isotopic compositions (‰) of anhydrite and gypsum from the Zhaoanzhuang iron deposit. (Abbreviations: Anh, anhydrite; Gp, gypsum; Lz, lizardite; Cal, calcite; Mhb, magnesiohornblende; Ms, muscovite; Zrn, zircon; Tlc, talc; and Py, pyrite).

Sample No.	Mineralogy	Sulfate Minerals		$\Delta^{33}S_{v\text{-}CDT}$
		$\delta^{34}S_{v\text{-}CDT}$	$\delta^{33}S_{v\text{-}CDT}$	
ZAZ14-6	97.2% Anh, 2.8% Gp	+21.1	+10.5	−0.31
ZAZ14-7	57.7% Anh, 42.3% Gp	+21.2	+10.7	−0.16
ZAZ14-10	100.0% Gp	+21.2	+10.5	−0.36
	Replicate	+21.4	+10.6	−0.36
ZAZ14-11	100.0% Gp	+21.2	+10.7	−0.16
	Replicate	+21.3	+10.6	−0.31
ZAZ14-13	85.6% Gp, 5.0% Anh, 3.8% Cal, 5.6% Lz	+21.3	+10.8	−0.11
ZAZ14-14	100.0% Gp	+21.8	+11.3	+0.13
ZAZ14-16	48.4% Gp, 51.6% Anh	+22.5	+11.5	−0.02
ZAZ14-18	98.0% Gp, 2.0% Anh	+21	+10.4	−0.36
ZAZ14-19	100.0% Gp	+22.5	+11.2	−0.32
ZAZ14-21	94.3% Gp, 5.7% Anh	+21	+11.1	+0.34
ZAZ14-23		+21.4	+11	+0.04
ZAZ14-24	98.8% Gp, 1.2% Anh	+21	+10.4	−0.36
ZAZ14-25	74.9% Gp, 22.6% Anh, 2.5% Cal	+21.3	+11.1	+0.19
	Replicate	+21.4	+10.9	−0.06
ZAZ14-26	98.1% Gp, 1.9% Mhb	+21.4	+11.3	+0.34
ZAZ14-27	100.0% Gp	+20.9	+10.7	−0.01
ZAZ14-29	100.0% Gp	+20.7	+10.9	+0.29
ZAZ14-30		+19.8	+9.8	−0.35
ZAZ14-35	100.0% Gp	+20	+10.3	+0.05
ZAZ14-37	96.9% Gp, 3.1% Lz	+21.3	+14.2	+3.29
ZAZ14-38	100.0% Gp	+20.3	+11.3	+0.9
ZAZ14-39	68.0% Gp, 30.2% Anh, 1.8% Mhb	+21.2	+11.6	+0.74
ZAZ14-40	72.6% Gp, 27.4% Anh	+20	+10.4	+0.15
	Replicate	+20	+10.3	+0.05
ZAZ14-41	67.1% Gp, 32.9% Anh	+20.1	+10.3	0
ZAZ14-42	100.0% Gp	+21.6	+10.9	−0.17
ZAZ14-43	100.0% Gp	+21.3	+11.3	+0.39
ZAZ14-46	100.0% Gp	+21.1	+11.1	+0.29
ZAZ14-47	97.1% Gp, 2.9% Anh	+20.8	+11	+0.34
ZAZ14-49	88.6% Gp, 11.4% Anh	+22.3	+11.6	+0.18
ZAZ14-54	100.0% Gp	+20.9	+11	+0.29
ZAZ14-55	92.7% Gp, 0.7% Lz, 6.6% Ms	+19.9	+10.4	+0.2
ZAZ14-57	100.0% Gp	+22.4	+11	−0.47
ZAZ14-58	91.0% Gp, 9.0% Ms	+20.6	+10.6	+0.04
ZAZ14-60	99.1% Gp, 0.9% Zrn	+20.8	+10.4	−0.26
ZAZ14-62	100.0% Gp	+20.5	+10.2	
ZAZ14-63	98.7% Gp, 1.3% Tlc	+20.8	+10.4	
ZAZ-13	Py	+11.5		
ZAZ-15	Py	+13.9		

Mg-rich iron ores and wall rock samples were collected from the drill hole ZK3211 and underground mining pits for Mg isotopic analyses. Two samples of serpentine–magnetite ores (ZAZ-11, ZAZ13-12), one sample of magnetite–serpentinite (ZK3211-29), and four wall rock samples, i.e., carbonate–magnetite–serpentinite (ZK3211-61), amphibolite (ZK3211-13), anhydrite–serpentinite (ZK3211-25), and serpentinized olivine–orthopyroxenite (ZAZ-25) were analyzed (Table 2 and Table S1). In these samples, the dominant Mg-bearing minerals are serpentine, olivine, orthopyroxene, hornblende,

and minor carbonate minerals. The serpentine is thought to be derived from the olivine and orthopyroxene, and it has been reported that serpentinization does not affect the Mg isotopic composition [109]. Therefore, the whole-rock magnesium isotopes can be used to constrain the Mg isotopic compositions of these magnesium-rich silicate minerals.

Table 2. Mg isotopic compositions (‰) of reference materials and representative magnesium silicate-rich rocks from the Zhaoanzhuang iron deposit.

Sample No.	Rock Type	δ^{26}Mg	2SD	δ^{25}Mg	2SD	Δ^{25}Mg
AGV-2	standard	−0.15	0.03	−0.06	0.01	0.02
BHVO-2	standard	−0.25	0.04	−0.11	0.04	0.02
ZAZ-11	magnetite–serpentinite	−0.93	0.02	−0.48	0.04	0.01
ZAZ-25	serpentinized olivine–orthopyroxenite	−0.80	0.02	−0.40	0.01	0.02
ZAZ13-12	magnetite–serpentinite	−0.66	0.06	−0.34	0.01	0.01
ZK3211-13	amphibolite	−0.34	0.03	−0.18	0.01	0.00
ZK3211-25	anhydrite–serpentinite	−1.20	0.06	−0.62	0.03	0.00
ZK3211-29	magnetite–serpentinite	−0.66	0.04	−0.34	0.01	0.00
ZK3211-61	dolomite–magnetite–serpentinite	−1.00	0.04	−0.52	0.01	0.00

Three tourmaline-rich rock samples (ZK2704-10, ZK2151-12, and ZK2151-23) with different lithologies, were collected from two drill holes (ZK2704 and ZK2151) for in situ B isotopic analysis using a laser ablation multi-collector inductively coupled mass spectrometer (LA-MC-ICPMS). One layer of tourmaline-rich rock (Figure 5c) containing minor diopside, which is located between the overlying olivine–amphibolite and the underlying olivine–orthopyroxenite, occurs as coarse-grained greenish euhedral crystals within quartzite in drill hole ZK2704 (Figure 2). Two finely laminated tourmaline-rich rocks occur in drill hole ZK2151. The medium-grained tourmaline-rich rock sample ZK2151-23, which is located at the bottom of the serpentine–magnetite ore, contains minor phlogopite and talc (Figure 5a). A tourmaline-rich rock from sample ZK2151-12 is cut by several gypsum veins (Figure 5b) and occurs as intercalation within the olivine–orthopyroxenite layer.

4.2. Analytical Methods

4.2.1. Sulfur Isotopes

Anhydrite and gypsum were separated from the Zhaoanzhuang iron ores and crushed into 200 mesh for sulfur isotopic analysis. In order to exclude impurity effects and to ensure the accuracy of the analytical results, the mineral compositions of these samples were also analyzed using XRD powder diffraction prior to S isotopic analysis. The S isotopic analysis was conducted using the high-accuracy SF_6 method [110,111] and all of the experimental procedures were conducted at the Institute of Mineral Resources, Chinese Academy of Geological Sciences, Beijing. All of the anhydrite and gypsum samples were converted into Ag_2S using the chemical acid reduction method. Then, the sulfide minerals were collected, wrapped in aluminum foil, and placed in a nickel reaction tube connected to a vacuum system, in which the sulfide reacted with BrF_5 at 300–350 °C for about 14 h to completely convert the sulfur to SF_6. The SF_6 was then separated from the excess BrF_5 and other impurities by cooling the solution in a liquid nitrogen cold trap, and conducting cryogenic distillation and purification with dry ice-acetone slush at ca. −80 °C. After this, the sulfur was further purified using a gas chromatography column, which was 6 mm in diameter, 2.2 m long, and packed with 5 Å molecular sieve material, and a highly purified helium carrier gas with a flow rate of 30 mL/min. After the He was extracted by cooling it with liquid nitrogen, the SF_6 was transferred to a sample tube for analysis.

The multiple-sulfur isotope ratios of the SF_6 were measured using a Finnigan MAT 253 type mass spectrometer. The isotope ratios were measuring the mass/charge at 124, 128, 129, and 131 amu. After the SF_6 gas underwent chromatographic separation and purification, the $\delta^{33}S$ and $\delta^{34}S$ values obtained were determined to be satisfactory. Based on repetitive measurements of standard samples (V-CDT: Vienna Canyon Diablo Troilite), the precision of the $\delta^{33}S$ and $\delta^{34}S$ data were determined to be ± 0.10‰.

The composition of the sulfur isotopes is represented using traditional delta notation:

$$\delta^{34}S = [(^{34}S/^{32}S)sample/(^{34}S/^{32}S)V\text{-}CDT - 1] \times 1000; \quad (1)$$

$$\delta^{33}S = [(^{33}S/^{32}S)sample/(^{33}S/^{32}S)V\text{-}CDT - 1] \times 1000; \quad (2)$$

$$\Delta^{33}S = \delta^{33}S - 1000 \times [(1+\delta^{34}S/1000)0.515 - 1]. \quad (3)$$

4.2.2. Whole-Rock Magnesium Isotopes

The magnesium isotopic analysis was conducted at the State Key Laboratory of Geological Processes and Mineral Resources, China University of Geosciences (Beijing) (CUGB), following the experimental procedures established by [47,59] and [112]. The following is a brief description of the magnesium isotope analytical procedure.

All of the chemical procedures were carried out in a clean laboratory environment. Sample powders were dissolved in Savillex screw-top beakers in a concentrated HF-HNO_3 (3:1) mixture. Then, the solution was heated to 160 °C on a hotplate in a laminar flow exhaust hood until it became transparent. Then, the solution was evaporated to dryness at 140 °C. In order to achieve 100% dissolution and to remove the residual fluorides, the dried residues were refluxed with a concentrated HCl-HNO_3 (3:1) mixture and evaporated to dryness again. After this, the residues were refluxed with concentrated HNO_3 and were repeatedly evaporated to dryness. Finally, the samples were dissolved in 1 N HNO_3 in preparation for chromatographic separation.

Chemical separation of the Mg was conducted using cation exchange chromatography columns filled with Bio-Rad 200-400 mesh AG50W-X8 resin. The resin was rinsed multiple times with columns full of 4 N HCl and 18.2 MΩ Milli-Q water. Then, the columns were cleaned with >5 full columns of 1 N HNO_3 and 18.2 MΩ Milli-Q water. After this, 2 mL of the sample were loaded into the columns and eluted with 1 N HNO_3 following the procedure outlined in [47,59] and [112]. The final solutions were heated to dryness in a vented laminar-flow hood and were dissolved in 3% HNO_3 for the mass spectrometry analysis. At least one rock standard was processed through the columns with each set of samples. The Mg yield of the column separation process was greater than 99% and the total procedural blank was consistently less than 10 ng, requiring insignificant corrections to the samples' isotopic compositions.

The magnesium isotopic ratios were measured using the sample-standard bracketing method and a *Neptune plasma* MC-ICPMS in low-resolution mode. Details are given by [112]. The data are reported in the δ-notation relative to international reference material DSM3 [113]:

$$\delta^{26}Mg = [(^{26}Mg/^{24}Mg)_{Sample}/(^{26}Mg/^{24}Mg)_{DSM3} - 1] \times 1000; \quad (4)$$

$$\delta^{25}Mg = [(^{25}Mg/^{24}Mg)_{Sample}/(^{25}Mg/^{24}Mg)_{DSM3} - 1] \times 1000. \quad (5)$$

Two USGS Mg rock standards (BHVO-2 and AGV-2) were analyzed during the analytical procedure, yielding $\delta^{26}Mg$ values of −0.25 ± 0.04‰ (2SD) and −0.15 ± 0.03‰ (2SD), respectively (Table 2), which are in excellent agreement (within error) with previously published values (e.g., [48,59,114].)

4.2.3. In-Situ Boron Isotopic Analysis

The in-situ boron isotopic compositions of the tourmaline in the wall rocks of the Zhaoanzhuang iron deposit were measured in polished thin sections using a Neptune Plus MC-ICP-MS and a New Wave UP213 laser ablation system at the Institute of Mineral Resources, Chinese Academy of Geological Sciences, Beijing. The parameters of the instrument and detailed analytical procedures have been described by [115] and are only briefly summarized here. The laser ablation spot diameter was 50 μm with an output frequency of 8 Hz. The maximum actual output power was adjusted to reach 8 J/cm^2 and the He carrier gas was set to 0.8 L/min. Here, we used the sample-standard bracketing method to correct for the mass bias of the instrument and for isotopic fractionation. The standard used was

NIST SRM 951 boric acid from the National Institute of Standard Technology ($^{11}B/^{10}B_{NIST\ SRM\ 951}$ = 4.05003). Standard IAEA B4 ($\delta^{11}B$ value of −8.36 ± 0.58‰) from the International Atomic Energy Agency was used as the external standard to ensure optimum results. Standard IRM RB1 (a certified reference material, $\delta^{11}B$ = −12.97 ± 0.58‰) was used as an internal standard yielding a precision of 1% (2σ). The data were collected statically and simultaneously in cycles of 200 with an integration time of 0.131 s and an acquisition time of 27 s.

The boron isotope data are reported in $\delta^{11}B$ notation as follows:

$$\delta^{11}B = [(^{11}B/^{10}B_{Sample})/(^{11}B/^{10}B_{NIST\ SRM\ 951} - 1)] \times 1000 \quad (6)$$

5. Results

The S, Mg, and B isotopic compositions are listed in Tables 1–3, respectively, and in the supplementary data (Table S1).

Table 3. In-situ laser ablation multi-collector inductively coupled mass spectrometer (LA-MC-ICPMS) B isotopic compositions (‰) of tourmaline from the wall rocks of the Zhaoanzhuang iron deposit.

Sample No.	Spots	$\delta^{11}B$	Sample No.	Spots	$\delta^{11}B$	Sample No.	Spots	$\delta^{11}B$
ZK2151-12	1-1	+2.6	ZK2151-23	1-1	+3.3	ZK2704-10	1-1	−0.6
	1-2	+2.2		1-2	+0.2		1-2	−0.4
	1-3	+0.2		1-3	+2.0		1-3	−0.3
	1-4	−0.2		1-4	+1.8		1-4	+1.9
	1-6	+1.9		1-5	+3.1		1-5	+0.3
	1-7	+1.4		1-6	+3.2		1-6	+0.2
	1-8	+1.1		1-7	+3.3		1-7	+0.7
	1-9	+1.2		1-8	+3.0		1-8	+1.4
	1-10	+2.7		1-9	+2.3		1-9	+3.6
	1-11	+3.2		1-10	+1.8		1-10	+2.8
	1-12	+2.7		1-11	+2.4		1-11	+3.4
	1-13	+1.8		1-12	+2.1		1-12	+1.6
Average		+1.7			+2.4			+1.8

For all of the different proportions of gypsum to anhydrite in the samples, the $\delta^{34}S$ values range from +19.8‰ to +22.5‰ (Table 1) with an average of +21.1‰ (N = 35), which falls within the range of marine anhydrites ($\delta^{34}S$ of +15 to +30‰) [116–118]. Most samples show clear and variable mass independent fractionation with $\Delta^{33}S$ values of −0.47‰ to +3.29‰ and a maximum $\Delta^{33}S$ value of +3.29‰. However, sample ZAZ14-37, which is 96.9% gypsum and 3.1% lizardite, has significantly different values of −0.47‰ to +0.90‰. This value is likely incorrect and is excluded from latter discussion. On a plot of $\delta^{34}S$ versus $\Delta^{33}S$, no correlation is observed (Figure 7a).

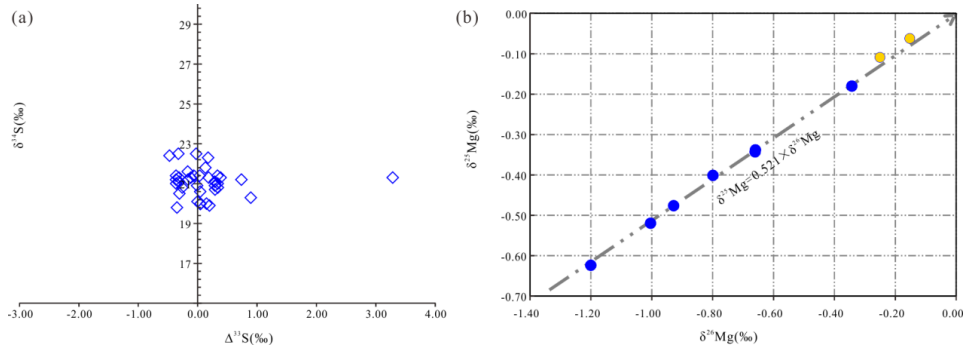

Figure 7. (**a**) Plot of $\delta^{34}S$ versus $\Delta^{33}S$ for the anhydrite and gypsum in the Zhaoanzhuang iron deposits. (**b**) Ternary magnesium isotope diagram of all of the samples (blue solid circles) and reference standards (yellow solid circles) analyzed in this study. The dashed line is the mass-dependent fractionation line with a slope of 0.521.

Because two of the standards and all of our samples fall on a straight line with a slope of 0.521 (Figure 7b) and the $\Delta^{25}Mg$ values ($\Delta^{25}Mg = \delta^{25}Mg - 0.521 \times \delta^{26}Mg$; [70]) range from 0 to 0.02‰ (Table 2), the Mg isotopic compositions obey the mass-dependent fractionation law, and thus, we only use $\delta^{26}Mg$ in the subsequent discussion. The Mg isotopic compositions fall within a limited range from −1.20‰ to −0.34‰ (Table 2) with an average of −0.80‰ (N = 7). The $\delta^{26}Mg$ values of all of the samples are significantly lower than the average values of chondrite ($\delta^{26}Mg = -0.25 \pm 0.07$‰) [47,59,69], except for sample ZK3211-13 ($\delta^{26}Mg = -0.34 \pm 0.03$‰). However, all of the samples fall within the wide range of marine carbonate rocks (–0.45‰ to −4.5‰) [50,119–121]. The carbonate–magnetite–serpentinite (ZK3211-61) and anhydrite–serpentinite (ZK3211-25) have the lowest $\delta^{26}Mg$ values, −1.00‰ and −1.20‰, respectively.

The in-situ boron analyses were performed on individual tourmaline grains from the tourmaline-rich rocks. The results reveal that the tourmaline grains from three different samples have $\delta^{11}B$ values ranging from −0.6‰ to +3.6‰ (Table 3). Three of the lower $\delta^{11}B$ values (1-1, 1-2, 1-3) for sample ZK2704-10 were excluded due to their low boron signal. Thus, the $\delta^{11}B$ values of the tourmaline fall within the narrow $\delta^{11}B$ range of −0.2‰ to +3.6‰ with an average of +2.0‰ (N = 33). The tourmaline intergrown with phlogopite and talc in sample ZK2151-23 has the highest average $\delta^{11}B$ of +2.4‰ (N = 12). The $\delta^{11}B$ values of the tourmaline are consistent with those of tourmaline from marine evaporite and carbonated-associated reservoirs ranging from −8.13‰ to +18.32‰ with an average of +1.37‰ (Table S1; [77]).

6. Discussion

6.1. The Source of Sulfur and the Role of Anhydrite in Mineralization

The $\delta^{34}S$ values of the anhydrite and gypsum in the Zhaoanzhuang iron deposit are homogeneous and show no correlation with their volume proportions, suggesting that no contamination or sulfur fractionation occurred during the late fluid stage. Thin-section observations indicate that abundant anhydrite occurs with serpentine, olivine, dolomite, apatite, and magnetite in the ores (Figure 3), but occurs with olivine, orthopyroxene, hornblende, and dolomite in the wall rocks (Figure 4). In addition, several other S-bearing minerals were observed in these rocks. These minerals probably crystallized during high-grade metamorphic evolution. The planar crystal boundaries between the anhydrite and other minerals indicate that the anhydrite is a metamorphic mineral, rather than the product of late hydrothermal alteration or an exotic fluid phase. It is considered that the anhydrite coexisted with dolomite, calcite, and apatite during the earlier prograde metamorphic stage. Therefore, the sulfur isotopes of the anhydrite can be used as indicators of the sulfur isotopic compositions ($\delta^{34}S$) of the original ore-forming materials. The $\delta^{34}S$ values of +19.8‰ to +22.5‰ (Table 1) with an average of +21.1‰ are comparable to the isotopic compositions of seawater sulfate (+21‰) [117,122–125], but are significantly higher than those of igneous sulfur ($\delta 34S = 0 \pm 5$‰) [31–33] and magmatic anhydrite ($\delta^{34}S = 0 \pm 5$‰). Magmatic anhydrite is a scarce primary igneous phase that occurs in oxidized intermediate and granitic magmatic systems [126,127] and has igneous sulfur isotopic compositions [127].

Additionally, two $\delta^{34}S$ values from pyrite (Table 1 and Table S1), which is a minor component of the Zhaoanzhuang iron deposit, are much higher (+11.5‰ and +13.9‰) than those of magmatic sulfides (close to zero) [31–35]. It is well known that sulfur from ultramafic sulfide minerals and high-$\delta^{34}S$ anhydrite cannot have such heavy sulfur isotopes [31–33] because of the mass balance in magmatic reservoirs with chondritic sulfur values. Therefore, the sulfur in the anhydrite and gypsum is more likely to have been derived from marine sediments.

Most processes on Earth that fractionate sulfur isotopes are proportional to their relative mass differences ($\Delta^{33}S = 0$) [37], and deviations from this relationship are commonly referred to as mass-independent fractionation ($\Delta^{33}S \neq 0$) [40,128]. Because high-temperature processes are not known to produce significant changes in $\Delta^{33}S$ [129], this mass-independent fractionation pattern is widely attributed to photodissociation of SO_2 by ultraviolet (UV) light in the presence of the extremely

low levels of O_2 and O_3 in Earth's Archean and Paleoproterozoic atmosphere [40,130,131]. Nevertheless, in an oxic atmosphere, mass-independent sulfur fractionation is also possible when large volcanic eruptions emit SO_2 directly into the stratosphere where the solar UV flux is high [132]. Consequently, the sulfate produced by photolysis of SO_2, which has negative $\Delta^{33}S$ values, precipitates near the volcanic center because it dissolves easily and is removed from the atmosphere by rain. Whereas, the insoluble S, which has positive $\Delta^{33}S$ values, is deposited far away from the volcanic center [40].

The sulfur in the anhydrite and gypsum in the Zhaoanzhuang iron deposit has variable $\Delta^{33}S$ values ranging from −0.47‰ to +0.90‰. Contamination by later sulfur input of any form, in the laboratory or the field, can be ruled out because it would not carry a substantial mass-independent sulfur fractionation signal [133]. Thus, the fact that significant mass-independent sulfur fractionation was recorded by the Zhaoanzhuang iron deposit, which is consistent with the conditions of the Early Archean-Paleoproterozoic atmosphere, supports the idea of an ancient exogenic sulfur cycle [44–46].

Furthermore, anhydrite and gypsum occur in two isotopically distinct populations, which have relatively constant negative $\Delta^{33}S$ values (−0.47‰ to −0.01‰) and more variable positive values (0‰ to +0.90‰), reflecting the mixing of two sulfur sources with distinct isotopic compositions. A similar situation caused the sulfur isotope pattern of the pyrite in the 2.5 Ga Klein Naute Formation in South Africa [134]. In addition, the ocean at that time would have appropriately mixed more than one sulfur reservoir in such a way as to preserve the reservoirs' mass-independent sulfur fractionation signatures [134]. However, the positive $\Delta^{33}S$ values of the anhydrite and gypsum in the Zhaoanzhuang deposit are quite prominent and exhibit a large range of values that deviate significantly from zero. As suggested by [135], sulfide minerals with a large range of $\Delta^{33}S$ (+1.55‰ to +1.21‰) from the banded iron formations (BIFs) of the North China Craton also show obvious signs of mass-independent sulfur fractionation. In fact, 80% of the superior-type BIF samples deposited in passive margin sedimentary environments [136] have positive $\Delta^{33}S$ values, whereas 90% of the Algoma-BIF samples associated with volcanic rocks [136] have negative $\Delta^{33}S$ values. The anhydrite and gypsum in the Zhaoanzhuang iron deposit display $\Delta^{33}S$ values similar to those of the superior-type BIFs. Thus, these minerals most likely formed in a passive margin basin far away from the volcanic center. Due to the long excursion distance, the S produced by photochemical reactions would likely be oxidized and settle into the ocean in the form of sulfate.

Sulfur can be used to trace the environment from which the ores precipitated, and the presence of multiple sulfur isotopic compositions indicates an ancient external source for the sulfur of the Zhaoanzhuang iron deposit. As shown in Table S1 from [137], sulfides from iron oxide-dominated deposits have relatively high $\delta^{34}S$ values ranging from −7.9‰ to +30‰, which are interpreted to represent evaporite-sourced sulfur. Therefore, the high sulfur isotopic features of the sulfide and sulfate minerals in the Zhaoanhzhuang deposit are probably derived from the evaporites.

Many iron oxide ores, including skarns, iron oxide-apatite (IOA), and iron oxide–copper–gold (IOCG) deposits, are associated with gypsum beds, which are interpreted to have played a critical role in the formation of iron oxide ore deposits by providing a major oxidizing agent [125,137,138]. The anhydrite in the Zhaoanzhuang iron deposit could be a pristine mineral, along with earlier dolomite, apatite, and calcite, which triggered the formation of abundant Fe^{3+} and relatively little Fe^{2+} in favor of magnetite precipitation.

6.2. The Source of Magnesium

Mg-rich iron deposits (or Mg–Fe deposits) can form through mafic-ultramafic magmatic processes, hydrothermal metasomatic processes, or chemical sedimentation. Thus, magnesium can be derived from magmatic, hydrothermal, or sedimentary sources. As can be seen from Figure 8, the $\delta^{26}Mg$ values of the mantle (−0.25 ± 0.07‰) [47] and modern seawater (−0.83 ± 0.09‰; [139]) are constant. The magnesium isotopes for mantle peridotites, pyroxenites, the various basaltic rocks that form from them, and normal eclogite produced from metamorphic genesis, are remarkably homogeneous,

suggesting that no significant fractionation occurs during mantle melting, magma differentiation, and high-temperature metamorphic dehydration [47,59–66].

Several studies confirmed mantle heterogeneity of mantle-derived carbonated eclogites, garnet–websterites, and phlogopite–pyroxenites, which have lower δ^{26}Mg values ranging from −1.93‰ to −0.43‰ [140,141]. These lower values are the result of mantle metasomatism by subducted oceanic slab fluids and the recycling of sedimentary carbonates with light δ^{26}Mg [142]. In addition, magmatic carbonatites also show dominant mantle-like Mg isotopic compositions and some have even higher δ^{26}Mg values due to Mg isotopic fractionation caused by silicate–carbonate liquid immiscibility and fractional crystallization of carbonate melts [143]. In contrast, sedimentary carbonate rocks have variable, lower Mg isotopic values compared to those of igneous rocks. Limestones generally have a lighter Mg isotopic composition (δ^{26}Mg < −2.5‰) than dolostone and marlstone [119]. Dolostones have a relatively large range of δ^{26}Mg values spectrum from −2.49‰ to −0.45‰ [119], while the δ^{26}Mg values of normal marine sedimentary dolostone range from −2.29‰ to −1.09‰ [50,120]. Due to differences in their Mg sources, precipitation environment, early diagenetic pathways, and other factors, the various types of dolostones have varying Mg isotopic compositions [119].

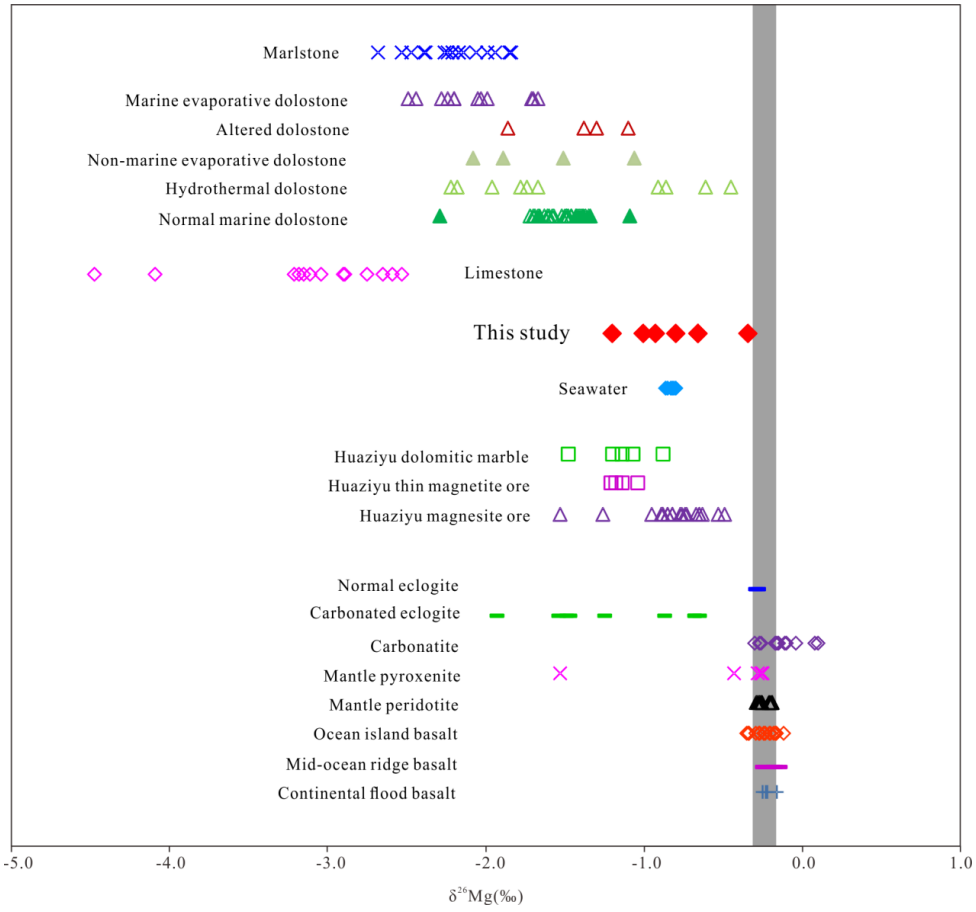

Figure 8. Compilation of Mg isotope data for the Zhaoanzhuang iron deposit and published data for carbonate rocks, igneous rocks, and modern seawater for comparison. The modern seawater data are from [61,70,144]. The marlstone data are from [121]; the limestone data are from [50,121], the normal marine dolostone data are from [50,119,120]; and all of the other dolostone data are from [119]. The Huaziyu magnesite and dolomitic marble data are from [145]. The igneous rock data are from [60,61,141,143]. The normal eclogite and carbonated eclogite data are taken from [140]. The solid grey vertical band represents the chondritic δ^{26}Mg value of −0.25 ± 0.07‰ [47,59].

Because metamorphic dehydration [64,66,73] and serpentinization [109] result in insignificant amounts of Mg isotopic fractionation, the δ^{26}Mg values of the seven samples analyzed in this study

can potentially reflect the primitive Mg isotopic composition of the Zhaoanzhuang iron deposit. These samples have whole-rock δ^{26}Mg values ranging from −1.20‰ to −0.34‰, which is inconsistent with the magnesium isotopic compositions of magmatic rocks, but falls into the range of dolostone values (δ^{26}Mg = −2.49‰ to −0.45‰) (Figure 8; [119]), and is approximately 0.7‰ higher than that of normal marine sedimentary dolostones (−2.29‰ to −1.09‰; [50,120]).

Metasomatic mantle-derived rocks, such as carbonated eclogites, garnet–websterite, and phlogopite–pyroxenite, also have light Mg isotopic compositions. This is due to the fact that sedimentary carbonate rocks have low δ^{26}Mg values, so metasomatism of the mantle by the addition of silicate melts and/or sedimentary carbonate-bearing fluids from an ancient subducted oceanic slab lowers the Mg isotopic composition of the mantle-derived rocks [64,141].

Therefore, if the Mg in the Zhaoanzhuang iron deposit was sourced from ultramafic magma, these low δ^{26}Mg values are most likely the result of mixing with sedimentary carbonate or carbonate-bearing fluid. The possible mixing processes could be due to either subduction of an oceanic slab into the mantle [140–142] or the intrusion of mantle melts into carbonate strata. The former process can be excluded because it requires a specific tectonic environment and makes a relatively small volume contribution [141], which is often recorded in mantle xenoliths and/or evolved continental and island arc basalts [142]. However, the latter process provides a possible explanation. The well-known skarn mineralization model shows that the mixing of Mg-rich, ^{26}Mg-depleted dolomitic wallrock and Mg-poor, ^{26}Mg-enriched magma can produce the observed low Mg isotopic signatures [146]. The associated intrusive body is most likely the series of olivine–orthopyroxenite, orthopyroxenite, or hornblendite bodies widely distributed throughout the Zhaoanzhuang iron orebodies. However, the alteration zone produced by the intrusion of magmatic material into the wallrock should result in a well-developed skarn mineralization system, which is not observed in the cross-sections or stratigraphic column of the Zhaoanzhuang iron orebody (Figure 2). Skarn-type deposits associated with ultramafic rocks and such water-salinity-poor hydrothermal fluid are very rare, and none of the other intermediate-silicic intrusive bodies more commonly associated with skarn-type deposits were observed. Thus, the mixing of the isotopically heavy Mg of the magma with the isotopically light Mg of the carbonate wall rock is unlikely to be responsible for the ^{26}Mg values of the Zhaoanzhuang iron deposit.

Hence, it is reasonable to speculate that the magnesium in the Zhaoanzhuang iron deposit was derived from marine carbonate sediments or a metasomatic hydrothermal fluid that sourced from the surrounding Mg-bearing rocks or Mg-rich brines during its precipitation. This is further supported by the presence of residual dolomite in the carbonate–magnetite ores and the weakly mineralized olivine–marble. The hydrothermal and sedimentary processes that occurred were not mutually exclusive [66]. The δ^{26}Mg values (mean value: −2‰; Table S1) of the dolomitic marble samples from the Tieshanmiao formation, which overlies the Zhaoanzhuang formation, are lower than the samples analyzed in this study; the Mg of the Zhaoanzhuang iron deposit could not have been solely derived from Mg-rich seawater. In addition, a hydrothermal fluid with a heavier Mg isotopic composition was also thought to play a significant role in dolomite precipitation. The amphibolite (ZK3211-13), which has a high mantle-like δ^{26}Mg, would be more intensely affected by this hydrothermal fluid. In addition, the δ^{26}Mg values of the Zhaoanzhuang iron deposit are consistent with those of the Paleoproterozoic Huaziyu magnesite deposit in the Liaohe Group of the northeastern margin of the North China Craton. Additionally, they are also consistent with those of the Paleoproterozoic dolomites in the Tulomozero formation in the Onega Basin along the southeastern Fennoscandian Shield, in Russia [55,145], both of which have values of about −0.8 ± 0.2‰ (Figure 9).

Based on the lithologies of the rocks in the study area, the coexisting Mg-rich carbonates (dolomite and magnesite) and gypsum or anhydrite in the Huaziyu area and in the Onega Basin are indicative of an evaporative environment or a coastal playa (sabkha) [55,145,147], in which pristine Mg-rich carbonate minerals, anhydrite, and B-rich minerals formed. Thus, seawater evaporation and the contemporaneous precipitation of marine carbonates and calcium sulfates (gypsum, anhydrite) are the

primary causes of the heavy Mg isotope enrichment of the rocks in the study area. The enrichment in the heavier ^{26}Mg can be explained by Rayleigh fractionation of the Mg isotopes in continuous evaporating of seawater in a closed system due to the ongoing precipitation of calcium sulfates and carbonates [55].

Consequently, the most probable source of Mg for the Zhaoanzhuang ore-forming material is dolomite or another magnesium-rich carbonate precipitated from Mg-rich seawater. Unfortunately, these carbonates have been almost completely transformed into magnesium silicate minerals (olivine, orthopyroxene, hornblende, and clinohumite) by upper amphibolite to granulite facies metamorphism.

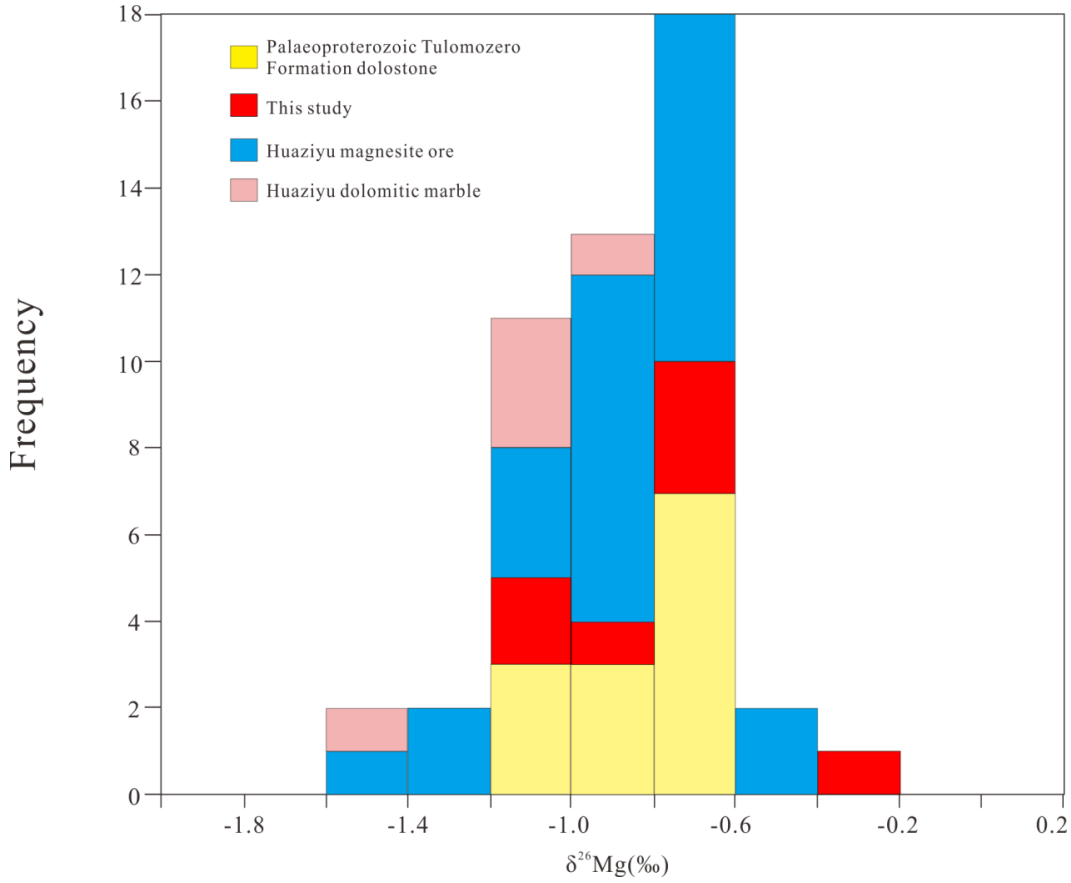

Figure 9. Histogram showing the δ^{26}Mg variations of the Zhaoanzhuang iron deposit (in this study) along with other published data for the sedimentary dolomites in the Palaeoproterozoic Tulomozero formation in the Onega Basin, southeastern Fennoscandian Shield, Russia [55] and the Huaziyu magnesites in the Palaeoproterozoic Lieryu formation in the Liaohe Group, northeastern North China Craton, China [145].

6.3. Boron Isotopes in Tourmalinite

In general, magmatic boron sources typically have negative δ^{11}B values, while the δ^{11}B isotopic values (Figure 10) of the primitive mantle (−9.9‰; [148]), bulk continental crust (−9.1‰; [149]), and mid-ocean ridge basalts (MORB = −7.1‰; [149]) vary slightly. However, altered magmatic rocks and serpentinized ultramafic rocks have slightly enriched B concentrations and higher δ^{11}B values than normal magmatic rocks due to interaction with ^{11}B-enriched seawater [85]. It has been experimentally determined that large B isotopic fractionation (up to +30‰) [150] occurs during supergene evaporative processes, which is consistent with the very high δ^{11}B values of natural brines (up to +59‰) from several salt lakes [79]. The high δ^{11}B values of marine precipitated evaporites and borate evaporate deposits (up to +25‰) [75] reflect the abundance of heavy ^{11}B in seawater (Figure 10; [144]).

As can be seen from Figure 10, tourmaline associated with marine evaporite- or carbonate-derived B sources can produce high δ^{11}B values, ranging from −8.1‰ to +18.3‰ [77]. The tourmalinites in the Early Archean Barbeton greenstone belt in South Africa also have high ^{11}B concentrations (Figure 10) due to input from a marine evaporitic B source with δ^{11}B ranging from +20‰ to +30‰ [151]. However, the δ^{11}B values of non-marine evaporite-associated, metavolcanic-associated, and clastic-associated tourmaline [71] have δ^{11}B values lower than those of marine evaporite- or carbonate-derived tourmaline.

In addition, the tourmaline that is frequently present in pegmatites formed from highly fractionated residual magmatic fluids enriched in mobile and incompatible B, which were released as the granitic pluton cooled [76]. The tourmaline in the rare-element pegmatites in Borborema Province in Brazil have a wide range of δ^{11}B from −20.2‰ to +1.6‰, which is similar to the range of worldwide pegmatite tourmalite [152]. The large B-isotopic fractionation in pegmatites could be due to their low solidus temperatures, high volatile contents, small magma volumes, and the occurrence of mineral segregation, fluid immiscibility, and exsolution [153]. The higher δ^{11}B values of the tourmaline in pegmatites are interpreted to be due to mixing of the magma with the heavy B from country rocks such as marble and calc-silicate rocks [152]. Due to complexity of the boron sources of natural rocks, tourmaline from various origins yields a wide preferentially negative δ^{11}B range of −30‰ to +22‰ [76,77,90].

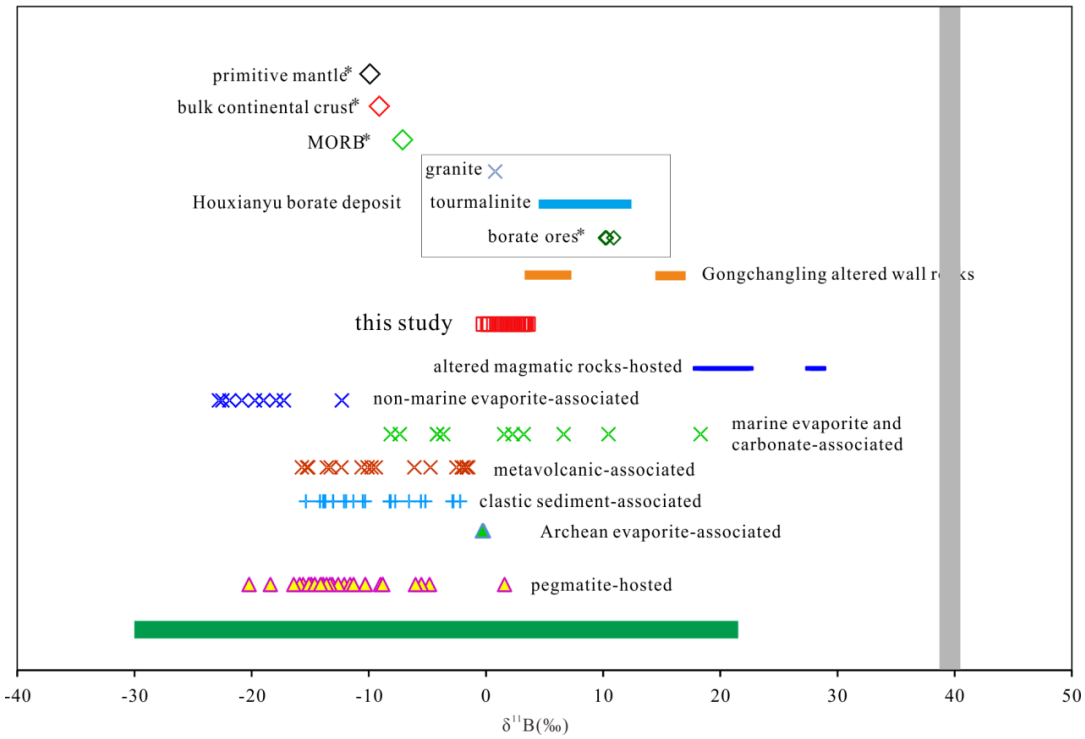

Figure 10. Comparison of the tourmaline δ^{11}B values of the interlayered tourmaline-rich rocks in the Zhaoanzhuang iron deposit with compiled data for non-marine evaporite-associated [154], marine evaporite and carbonate-associated [77], metavolcanic-associated [154], clastic sediment-associated [154], Archean evaporite-associated [151], altered magmatic rocks-associated [85], and pegmatite-hosted [152] tourmaline. The tourmaline δ^{11}B values of the tourmalinite and granite in the Houxianyu borate deposit, northeastern North China Craton [155,156] and the altered wall rocks in the Gongchangling high-grade iron ore deposit, Anshan-Benxi area of the North China Craton (Wang Qian, unpublished data) are also plotted for comparison. Houxianyu borate deposit data with * symbol indicate δ^{11}B values of borate ores [155]. Data with * symbol indicate the average δ^{11}B composition of the primitive mantle [148], bulk continental crust [149], and uncontaminated mid-ocean ridge basalts (MORB) [149]. The solid green lateral band represents the δ^{11}B variations of tourmaline in natural rocks [76,77,90]. The solid grey vertical band represents a δ^{11}B value of +39.6 ± 0.04‰ [144].

The tourmaline from the Zhaoanzhuang iron deposit formed during the metamorphic stage at high temperatures of 700–750 °C [102,106], rather than as a product of the hydrothermal stage. This is supported by its unzoned texture and the fact that it is cut by gypsum veins. The tourmaline's unzoned texture could indicate that the tourmaline was not crystallized during the progressive metamorphic stage because tourmaline formed during the prograde stage generally retains its zoned structure due to evolving *P-T-X* conditions and negligible intracrystalline element diffusion over geologic time frames, even at temperatures in excess of 600 °C [85,157].

Some of the iron ores and wall rocks have B contents of 60 to 200 ppm (Table S1), which is significantly higher than those of primitive mantle and depleted mantle, 0.19 and 0.077 ppm, respectively [149]. Thus, we conclude that the boron was leached from the host rocks through dehydration reactions during prograde metamorphism, and then, the B as well as abundant Mg, Al, Fe, and Ca were used to form tourmaline at a high temperature during peak metamorphism.

Tourmaline from three samples from the Zhaoanzhuang iron deposit have a narrow range of in situ $\delta^{11}B$ values of −0.2‰ to +3.6‰ with a mean value of +2‰ (N = 33) (Table 3), which differs from the wide ranges of $\delta^{11}B$ values seen in tourmaline from other environments, such as magmatic rocks, metavolcanic and sedimentary rocks, and marine and non-marine evaporites (Figure 10). The similarity of the $\delta^{11}B$ values of tourmaline phenocrysts with different lithologic features from the three samples suggests that these tourmaline-rich rocks have a common boron source, which could be the main factor controlling the B isotopic composition of tourmaline that underwent limited boron isotopic fractionation at a high temperature [83].

However, the temperature dependence of the boron isotopic fractionation factor between tourmaline and aqueous fluid/vapors is also significant, which is supported by experimental results [83,158]. The $\delta^{11}B$ values of the tourmaline must be lower than that of the fluid from which it precipitated, in order for the preferential fractionation of ^{11}B into the fluid to occur. Palmer et al. [83] produced experimental B isotopic fractionation of 2‰ to 6‰ at a temperature of 750 to 350 °C; while Meyer et al. [158] produced 0.8‰ to 2.7‰ fractionation at 700 to 400 °C. In order to determine the boron source, the $\delta^{11}B$ value of the tourmaline must be corrected for fractionation between the fluids and minerals ($\Delta^{11}B_{tourmaline\text{-}fluid}$). According to the equation for equilibrium boron fractionation, $\Delta^{11}B_{tourmaline\text{-}fluid} = -4.20 \times [1000/T\ (K)] + 3.52$ determined by [158], the $\delta^{11}B$ values of the fluid be +0.4‰ to +4.4‰ at temperatures of 750 to 700 °C.

Thus, the isotopically heavy boron was likely derived from a high $\delta^{11}B$ carbonate source. This, combined with the high B contents of the deposit, suggests a marine evaporite component. Comparable ($\delta^{11}B$ = +3.3‰ to +7.3‰) and even higher $\delta^{11}B$ ($\delta^{11}B$ = +14.5‰ to +17‰) values (Figure 10, unpublished data from Wang Qian) were recorded in tourmaline phenocrysts from the altered wall rocks adjacent to the Gongchangling high-grade iron ores in the Anshan area, in the northeastern part of the North China Craton. These heavy boron isotopes are believed to have leached from the evaporite layer in the Liaohe Group. In addition, tourmalinite and borate ores in the Houxianyu Mg–Fe-rich borate deposit in the Liaohe Group also have heavy boron isotopic compositions (Figure 10), which was likewise interpreted to be the result of interaction with Mg-rich marine carbonates and evaporites [155,156]. However, the lack of boron minerals and the lower $\delta^{11}B$ values of the tourmaline in the Zhaoanzhuang iron deposit compared to those in the Gongchangling iron deposit and the Houxianyu Mg–Fe-rich borate deposit suggests that the Zhaoanzhuang iron deposit was precipitated from low $\delta^{11}B$ seawater in a weaker evaporitic environment.

6.4. Implications for Provenance and Metallogenic Processes

Petrographic observations reveal that the serpentine–magnetite ores were once olivine–(orthopyroxene)–magnetite Mg-rich iron ores. An Mg-rich iron deposit can be formed by mafic-ultramafic magmatic processes, hydrothermal metasomatic processes, or by chemical sedimentation. High-Mg iron deposits with a mafic-ultramafic origin are rarely seen in nature, especially olivine-bearing iron oxide deposits. However, this type of deposit is seen in the middle

petrographic zone of the Hongge layer intrusion and in the lower petrographic zone of the Baima layered intrusion in the Emeishan Large Igneous Province, southwestern China [159–161]. These examples are characterized by the occurrence of olivine with Fo values of 63–83 [162–164], clinopyroxene, and Fe–Ti oxides and higher MgO contents than those of other iron oxide deposits sourced from layered intrusions [164,165]. The large thickness of these olivine-rich magnetite ores is commonly considered to be due to the fact that they are derived from picritic primary magmas by fractionation crystallization of silicate minerals in deep magma chambers [166–169].

Magnesian skarn rock is a proxy for hydrothermal metasomatic genesis. Examples of this type of skarn include the Galinge iron-bearing magnesian skarn zone in the Qiman Tagh metallogenic belt, western Tianshan, China, which formed through the interaction between granodiorite and dolomitic marble [170], and the Janggun magnesian skarn-type iron deposits, Republic of Korea, which developed in the Cambrian dolomitized Janggun Limestone along its contact with the Jurassic Chunyang granite [171]. The gangue minerals in the ores mainly include Mg-rich forsterite, serpentine, chondrodite, clinochlore, talc, phlogopite, dipside, and carbonate minerals (dolomite, magnesite, and calcite), while the ore minerals include magnetite, hematite, pyrrhotite, and various other sulfides [171]. Chemical sedimentogenic Mg–Fe deposits were most commonly formed in the Precambrian and underwent various levels of late metamorphic or hydrothermal processes. These deposits include the Tianhu dolomite–pyrite–magnetite deposit hosted in the Neoproterozoic Tianhu Group in Eastern Tianshan [172,173], the Lilaozhuang magnesite–magnetite deposit within the Neoarchean-Paleoproterozoic Huoqiu Group [174–177], and the Lieryu magnesite–magnetite and borate deposits in the Paleoproterozoic Liaohe Group [66,178]. The latter two representative deposits of high-Mg chemical precipitation genesis are located on the southern and northern margins of the North China Craton (NCC), respectively (Figure 1a). The Lilaozhuang Mg–Fe ores formed in a confined sea basin on a continental margin [176], while the Lieryu boronmagnesite–magnetite deposits formed in a marine evaporative environment [66,155,156,179].

In the Zhaoanzhuang iron deposit, strong deformation and high-grade metamorphism obliterated many of the primary textural characteristics of the protolith. Thereby, different studies have proposed various theories for the origin of the Zhaoanzhuang iron ores and their host rocks. Previous models for the origin of these iron deposits mainly agree on an ultramafic intrusion origin [6,8–12,14,15]. However, purely ultramafic magmatic genesis can easily be discounted on the basis of the very negative and varied Mg isotopic compositions of the Zhaoanzhuang iron deposit (Table 2 and Table S1), which is inconsistent with the limited Mg isotopic fractionation produced during partial melting and crystal fractionation [47,59–61]. Despite the fact that these isotopic compositions do not entirely discount the possibility of intrusion-associated magnesian skarn-type deposits hosted in dolomitic carbonate rocks, based on the limited outcrops and the analyzed samples, we believe that magmatic skarn mineralization should be excluded as a possibility due to the following arguments: (1) There is no significant enrichment of any other base metal, which is common in other intrusion-associated skarn deposits [171,180,181]. (2) There is no alteration zonation, which is common in skarn mineralization systems when magma intrudes the wall rock. (3) No late metasomatic textures formed adjacent to the iron ores, such as greisenization, albitization, and epidotization, but these features are well-developed in skarns [182]. (4) Garnet and diopside are absent, but in skarns, these minerals commonly form along the contact zone. (5) No obvious mineralized endoskarns developed in the hornblende–oligoclase or garnet–hornblende–oligoclase gneiss underlying the iron orebodies (Figure 2), which if present, would represent fluid pathways from the intrusion into the overlying sedimentary rocks [183].

Thus, the magnesium-rich silicates in the Zhaoanzhuang deposit are metamorphic minerals formed from Si–Mg-rich carbonate minerals. This is supported by the occurrence of abundant residual dolomite in some of the ores and wallrocks. We conclude that the Zhaoanzhuang iron deposit was formed by metamorphism of Fe–Si–Mg-rich marine carbonate rocks, the original mineral compositions of which are difficult to completely determine due to their complete transformation by late-stage high-grade metamorphism. However, the Mg-rich chemical compositions of the initial ore-forming materials of

the Zhaoanzhuang iron deposit are consistent with carbonate-associated chemical sedimentogenic Mg–Fe deposits.

Examples of this type of deposit include the Tianhu dolomite–pyrite–magnetite deposit, the Lilaozhuang magnesite–magnetite deposit, and the Lieryu magnesite–magnetite–borate deposits. In addition, the Mg isotopic composition of the Zhaoanzhuang iron deposit is similar to that of Paleoproterozoic Mg-rich carbonate rocks (Figure 9). These features suggest that these superior-type IFs precipitated in a similar marine environment [136]. Tectonically, the Zhaoanzhuang, Lilaozhuang, and Lieryu Mg-rich iron deposits are located on the North China Cratonic margin, which may be a factor in their similar formation periods and marginal seawater environment.

However, except for the Lieryu iron deposit, few geochronological studies have been conducted on the Lilaozhuang and Zhaoanzhuang iron deposits. Most studies agree on a Paleoproterozoic formation time for the Lieryu Mg-rich iron deposits [66,145,178,184], but several studies determined Neoarchean formation time for the Lilaozhuang iron deposit [176,177]. The Zhaoanzhuang iron deposit is hosted in the Neoarchean-Paleoproterozoic Taihua Group [95–100], and the occurrence of mass-independent sulfur fractionation in the Zhaoanzhuang iron deposit is consistent with the Neoarchean-Paleoproterozoic anoxic atmosphere. The Lieryu iron deposit, which is hosted within Mg–silicate and Mg–carbonate rocks, is the most studied due to its abundant boron, magnesium, and iron. This deposit was formed by the metamorphism of marine evaporites [66,145,178,184]. The abundant anhydrite with very positive $\delta^{34}S$ (+21.1‰) and $\delta^{11}B$ values (+2.0‰) and high B contents in the serpentine–magnetite ores of the Zhaoanzhuang iron deposit and wall rocks suggest that the Zhaoanzhuang iron deposit also most likely formed in an evaporitic environment.

7. Conclusions

Petrography and S–Mg–B isotope geochemistry indicate that the serpentine–magnetite ores of the Zhaoanzhuang iron deposit have a chemical sedimentary origin, rather than an ultramafic intrusion-associated origin. The Zhaoanzhuang iron deposit is hosted in a series of Fe–Si–Mg-rich marine carbonate strata with considerable evaporitic components, which were precipitated in a Mg-rich marginal seawater evaporitic environment. The ore-forming mechanism involving the following processes: (1) Early diagenesis preserved the abundant ferrous iron components and the silica equivalents of the magnesium-rich carbonate rocks, and (2) regional metamorphic processes at 1.95–1.8 Ga triggered magnetite mineralization and transformed the magnesium-rich carbonate minerals into magnesium-rich silicates. The abundant anhydrite possibly played a critical role by oxidizing the ferrous iron during mineralization, leading to the precipitation of large amounts of magnetite. The Zhaoanzhuang iron deposit's high $\delta^{34}S$ (+21.1‰) and $\delta^{11}B$ (+2.0‰) values and low $\delta^{26}Mg$ values (−0.80‰) suggest that this deposit was formed in a marine evaporitic environment.

Supplementary Materials: The following are available online at http://www.mdpi.com/2075-163X/9/6/377/s1, Table S1: The collected and analytical S–Mg–B isotopic data and B contents from references and Zhaoanzhuang iron deposit in this study.

Author Contributions: Conceptualization, H.L. and Y.L.; methodology, Y.L.; software, J.M.; validation, J.M., L.L. and Z.S.; formal analysis, J.M.; investigation, J.M., L.L. and Z.S.; resources, H.L.; data curation, J.M.; writing—original draft preparation, J.M.; writing—review and editing, J.M. and Z.Z.; visualization, J.M. and Z.Z.; supervision, Z.Z.; project administration, H.L.; funding acquisition, H.L.

Funding: This study was fully funded by the Natural Science Foundation of China (grant number 41672078).

Acknowledgments: We thank Yuan-You Zhang for his help in the field work. We acknowledge De-Fang Wan, Ke-Jun Hou, Shan Ke, and Xu-Nan Meng for their help during isotopic analyses. We are grateful to three anonymous reviewers for their insightful comments and detailed suggestions that significantly improved the paper.

Conflicts of Interest: The authors declare no conflict of interest.

References

1. Meng, J.; Li, H.M.; Li, L.X.; Santosh, M.; Song, Z.; Yang, X.Q. Petrological and geochemical constraints on the protoliths of serpentine-magnetite ores in the Zhaoanzhuang Iron Deposit, southern North China Craton. *Acta Geol. Sin. (Engl. Ed.)* **2018**, *92*, 627–665. [CrossRef]
2. Luo, M.Q. Study on ore-controlling factors in Wuyang iron ore field in Henan Province. *J. Henan Polytech. Univ. (Nat. Sci.)* **2009**, *28*, 576–582. (In Chinese)
3. Jia, X.J.; Li, H.Q.; Zheng, H.J. Study on the geological characteristics and deep prospecting of iron deposits in Wuyang City, Henan Province. *Gold Sci. Technol.* **2012**, *20*, 25–31, (In Chinese with English Abstract).
4. Zhai, J.W. Metallogenic mode and prospecting direction of the Wuyang iron deposit, Henan Province. *West-China Explor. Eng.* **2012**, *1*, 127–130. (In Chinese)
5. Liu, L.X.; Li, H.Q.; Jia, X.J.; Wang, W.Z.; Wang, X. Geological characteristics and genesis of iron ores of Zhaoanzhuang Formation in Wuyang iron ore field of Henan. *Miner. Resour. Geol.* **2014**, *28*, 431–434, (In Chinese with English Abstract).
6. Yu, S.Y.; Zhuang, L.C.; Li, S.Z. Genesis and minerogenetic characteristics of the iron deposit of Zhaoanzhuang type in the Wuyang region, Henan Province. *Geochimica* **1983**, *11*, 71–79, (In Chinese with English Abstract).
7. Jiang, Y.N.; Chen, Y.H. A discussion on the genesis of Zhaoanzhuang iron ore deposit in Wuyang County, Henan Province. *Bull. Tianjing Inst. Geol. Miner. Resour.* **1986**, *16*, 1–64, (In Chinese with English Abstract).
8. Jiang, Y.N. A study of the lizardites in Zhaoanzhuang iron ore deposit at Wuyang County, Henan Province. *Geol. Prospect. Rev.* **1990**, *5*, 40–49, (In Chinese with English Abstract).
9. Jiang, Y.N. Study of fluor-apatite in Zhaoanzhuang iron ore deposit at Wuyang County, Henan Province. *Geol. Prospect. Rev.* **1991**, *6*, 58–66, (In Chinese with English Abstract).
10. Li, J.P.; Li, Y.F.; Xie, K.J. Geological characteristics and ore-controlling significance of the Wuyang Taihua Group, Henan Province. *Miner. Resour. Geol.* **2012**, *26*, 30–34, (In Chinese with English Abstract).
11. Wang, X. Geological Characteristics and Prospecting Potential of Wuyang Iron Ore, Wugang County, Henan Province. Master's Thesis, China University of Geosciences (Beijing), Beijing, China, 2013. (In Chinese with English Abstract).
12. Lan, C.Y.; Zhao, T.P.; Luo, Z.Z.; Wang, C.L.; Wen, Q.F.; Liu, L.X. The genesis of the Zhaoanzhuang Fe oxide deposit in Wuyang region of Henan Province: Insights from magnetite and apatite. *Acta Petrol. Sin.* **2015**, *31*, 1653–1670, (In Chinese with English Abstract).
13. Lan, C.Y.; Zhou, Y.Y.; Wang, C.L.; Zhao, T.P. Depositional age and protoliths of the Paleoproterozoic upper Taihua Group in the Wuyang area in the southern margin of the North China Craton: New insights into stratigraphic subdivision and tectonic setting. *Precambrian Res.* **2017**, *297*, 77–100. [CrossRef]
14. Tu, E.Z.; Zhang, H.W. Rock and mineral assemblage features and metallogenesis of ore-bearing layers in the Zhaoanzhuang Formation of the Wuyang iron mine, Henan Province. *J. Geol.* **2016**, *40*, 567–574, (In Chinese with English Abstract).
15. Zhang, K.; Shen, B.F.; Sun, F.Y.; Zhou, H.Y.; Li, H.K. Metallogenic epoch of Zhaoanzhuang iron ore deposit in Wuyang, Henan Province: Oldest magmatic type iron ore deposit in China. *Miner. Depos.* **2016**, *35*, 889–901, (In Chinese with English Abstract).
16. Yui, S. Decomposition of siderite to magnetite at lower oxygen fugacities: A thermodynamic interpretation and geological implications. *Econ. Geol.* **1966**, *61*, 768–776. [CrossRef]
17. Gieré, R. Titanian clinohumite and geikielite in marbles from the Bergell contact aureole. *Contrib. Mineral. Petrol.* **1987**, *96*, 496–502. [CrossRef]
18. Kurt, B.; Grapes, R. *Petrogenesis of Metamorphic Rocks*, 8th ed.; Spring-Verlag: Heidelberg, Germany; Dordrecht, The Netherlands; London, UK; New York, NY, USA, 2011; pp. 225–253.
19. Jin, S.Q.; Li, H.C. *Introduction to Genetic Mineralogy (the Second Volumn)—The Genetic Mineralogy of Several Kinds of Common Minerals*; Jilin University Press: Changchun, China, 1986; pp. 122–124. (In Chinese)
20. Meinert, L.D.; Dipple, G.M.; Nicolescu, S. World skarn deposits. *Econ. Geol.* **2005**, 299–336.
21. Bucher, P.K.; Grapes, R. Metamorphism of Dolomites and Limestones. In *Petrogenesis of Metamorphic Rocks*, 8th ed.; Springer: Berlin/Heidelberg, Germany, 2011; pp. 225–255.
22. Huang, F. Non-traditional stable isotope fractionation at high temperatures. *Acta Petologica Sin.* **2011**, *27*, 365–382, (In Chinese with English Abstract).

23. Zhao, G.C.; Wilde, S.A.; Cawood, P.A.; Sun, M. Archean blocks and their boundaries in the North China Craton: Lithological, geochemical, structural and P-T path constraints and tectonic evolution. *Precambrian Res.* **2001**, *107*, 45–73. [CrossRef]
24. Santosh, M. Assembling North China Craton within the Columbia supercontinent: The role of double-sided subduction. *Precambrian Res.* **2010**, *178*, 149–167. [CrossRef]
25. Li, H.M.; Zhang, Z.J.; Li, L.X.; Zhang, Z.C.; Chen, J.; Yao, T. Types and general characteristics of the BIF-related iron deposits in China. *Ore Geol. Rev.* **2014**, *57*, 264–287. [CrossRef]
26. Han, C.S. Analysis of the exploration perspective in the depth of Wuyang iron deposit, Henan Province. *Miner. Resour. Geol.* **2010**, *24*, 150–154, (In Chinese with English Abstract).
27. Li, H.Q. The attribution of basement rocks in Wuyang iron ore field in Henan province. *Miner. Resour. Geol.* **2012**, *26*, 119–122, (In Chinese with English Abstract).
28. Yao, T.; Li, H.M.; Li, W.J.; Li, L.X.; Zhao, C. Origin of the disseminated magnetite pyroxenite in the Tieshanmiao type iron deposits in the Wuyang region of Henan Province, China. *J. Asian Earth Sci.* **2015**, *113*, 1235–1252. [CrossRef]
29. Andreae, M.O. Chemical and stable isotope composition of the high grade metamorphic rocks from the Arendal Area, Southern Norway. *Contrib. Mineral. Petrol.* **1974**, *47*, 299–316. [CrossRef]
30. Zheng, Y.F. Sulfur isotopes in metamorphic rocks. *Neues Jahrb. fü Mineral. Abh.* **1990**, *161*, 303–325.
31. Ault, W.U.; Kulp, J.L. Isotopic geochemistry of sulphur. *Geochim. Cosmochim. Acta* **1959**, *16*, 201–235. [CrossRef]
32. Ohmoto, H.; Rye, R.O. Isotopes of sulfur and carbon. In *Geochemistry of Hydrothermal Ore Deposits*, 2nd ed.; Barnes, H.L., Ed.; John Wiley and Sons: New York, NY, USA, 1979; pp. 509–567.
33. Ohmoto, H. Stable isotopic geochemistry of ore deposits. *Rev. Mineral. Geochem.* **1986**, *16*, 491–559.
34. Zheng, Y.F. Sulphur isotopic fractionation between sulphate and sulphide in hydrothermal ore deposits: Disequilibrium vs equilibrium processes. *Terra Nova* **1991**, *3*, 510–516. [CrossRef]
35. Zheng, Y.F.; Chen, J.F. *Stable Isotopic Geochemistry*; Science Press: Beijing, China, 2000; pp. 1–316. (In Chinese)
36. Oeser, M.; Strauss, H.; Wolff, P.E.; Koepke, J.; Peters, M.; Garbe-Schönberg, D.; Dietrich, M. A profile of multiple sulfur isotopes through the Oman ophiolite. *Chem. Geol.* **2012**, *312–313*, 27–46. [CrossRef]
37. Hulston, J.R.; Thode, H.G. Variations in the S^{33}, S^{34}, and S^{36} contents of meteorites and their relation to chemical and nuclear effects. *J. Geophys. Res.* **1965**, *70*, 3475–3484. [CrossRef]
38. Young, E.D.; Galy, A.; Nagahara, H. Kinetic and equilibrium mass-dependent isotopic fractionation laws in nature and their geochemistry and cosmochemical significance. *Geochim. Et Cosmochim. Acta* **2002**, *66*, 1095–1104. [CrossRef]
39. Li, Y.H.; Hou, K.J.; Wan, Y.S.; Yue, G.L. Archean mass-independent fractionation of sulfur isotope: New evidence of bedded sulfide deposits in the Yanlingguan-Shihezhuang area of Xintai, Shandong Province. *Acta Geol. Sin.* **2008**, *82*, 444–450.
40. Farquhar, J.; Bao, H.M.; Thiemens, M. Atmospheric influence of Earth's earliest sulfur cycle. *Science* **2000**, *289*, 756–758. [CrossRef] [PubMed]
41. Thiemens, M.H. Mass-independent isotope effects in Planetary atmospheres and the early solar system. *Science* **1999**, *283*, 341–345. [CrossRef] [PubMed]
42. Thiemens, M.H. The mass-independent ozone isotope effect. *Science* **2001**, *293*, 226. [CrossRef] [PubMed]
43. Ono, S.H.; Eigenbrode, J.L.; Pavlov, A.A.; Kharecha, P.; Rumble, D.; Kasting, J.F.; Freeman, K.H. New insights into Archean sulfur cycle from mass-independent sulfur isotope records from the Hamersley Basin, Australia. *Earth Planet. Sci. Lett.* **2003**, *213*, 15–30. [CrossRef]
44. Bühn, B.; Santos, R.V.; Dardenne, M.A.; de Oliveira, C.G. Mass-dependent and mass-independent sulfur isotope fractionation ($\delta^{34}S$ and $\delta^{33}S$) from Brazilian Archean and Proterozoic sulfide deposits by laser ablation multi-collector ICP-MS. *Chem. Geol.* **2012**, *312–313*, 163–176.
45. Strauss, H. Sulphur isotopes and the early Archaean sulphur cycle. *Precambrian Res.* **2003**, *126*, 349–361. [CrossRef]
46. Johnston, D.T. Multiple sulfur isotopes and the evolution of Earth's surface sulfur cycle. *Earth-Sci. Rev.* **2011**, *106*, 161–183. [CrossRef]
47. Teng, F.Z.; Li, W.Y.; Ke, S.; Marty, B.; Dauphas, N.; Huang, S.C.; Wu, F.Y.; Pourmand, A. Magnesium isotopic composition of the Earth and chondrites. *Geochim. Cosmochim. Acta* **2010**, *74*, 4150–4166. [CrossRef]

48. An, Y.J.; Huang, F. A review of Mg isotope analytical methods by MC-ICP-MS. *J. Earth Sci.* **2014**, *25*, 822–840. [CrossRef]
49. Saenger, C.; Wang, Z.R. Magnesium isotope fractionation in biogenic and abiogenic carbonates: Implications for paleoenvironmental proxies. *Quat. Sci. Rev.* **2014**, *90*, 1–21. [CrossRef]
50. Galy, A.; Bar-Matthews, M.; Halicz, L.; O'Nions, R.K. Mg isotopic composition of carbonate: Insight from speleothem formation. *Earth Planet. Sci. Lett.* **2002**, *201*, 105–115. [CrossRef]
51. Tipper, E.T.; Galy, A.; Gaillardet, J.; Bickle, M.J.; Elderfield, H.; Carder, E.A. The magnesium isotope budget of the modern ocean: Contraints from riverine magnesium isotope ratios. *Earth Planet. Sci. Lett.* **2006**, *250*, 241–253. [CrossRef]
52. Pogge von Strandmann, P.A.E. Precise magnesium isotope measurements in core top planktic and benthic foraminifera. *Geochem. Geophys. Geosystems* **2008**, *9*, Q12015. [CrossRef]
53. Higgins, J.A.; Schrag, D.P. Constraining magnesium cycling in marine sediments using magnesium isotopes. *Geochim. Et Cosmochim. Acta* **2010**, *74*, 5039–5053. [CrossRef]
54. Teng, F.Z.; Li, W.Y.; Rudnick, R.L.; Gardner, L.R. Contrasting lithium and magnesium isotope fractionation during continental weathering. *Earth Planet. Sci. Lett.* **2010**, *300*, 63–71. [CrossRef]
55. Farkaš, J.; Chakrabarti, R.; Jacobsen, S.B.; Kump, L.R.; Melezhik, V.A. Ca and Mg isotopes in sedimentary carbonates. In *Reading the Archive of Earth's Oxygenation*; Melezhik, V.A., Ed.; Global Events and the Fennoscandian Arctic Russia: Drilling Early Earth Project; Springer: Berlin/Heidelberg, Germany, 2012; Volume 3, pp. 1468–1482.
56. Gao, T.; Ke, S.; Teng, F.Z.; Chen, S.M.; He, Y.S.; Li, S.G. Magnesium isotope fractionation during dolostone weathering. *Chem. Geol.* **2016**, *445*, 14–23. [CrossRef]
57. Li, W.Q.; Beard, B.L.; Li, C.X.; Xu, H.F.; Johnson, C.M. Experimental calibration of Mg isotope fractionation between dolomite and aqueous solution and its geological implications. *Geochim. Et Cosmochim. Acta* **2015**, *157*, 164–181. [CrossRef]
58. Wang, W.Z.; Qin, T.; Zhou, C.; Huang, S.C.; Wu, Z.Q.; Huang, F. Concentration effect on equilibrium fractionation of Mg-Ca isotopes in carbonate minerals: Insights from first-principles calculations. *Geochim. Et Cosmochim. Acta* **2017**, *208*, 185–197. [CrossRef]
59. Teng, F.Z.; Wadhwa, M.; Helz, R.T. Investigation of magnesium isotope fractionation during basalt differentiation: Implications for a chondritic composition of the terrestrial mantle. *Earth Planet. Sci. Lett.* **2007**, *261*, 84–92. [CrossRef]
60. Yang, W.; Teng, F.Z.; Zhang, H.F. Chondritic magnesium isotopic composition of the terrestrial mantle: A case study of peridotite xenoliths from the North China Craton. *Earth Planet. Sci. Lett.* **2009**, *288*, 475–482. [CrossRef]
61. Bourdon, B.; Tipper, E.T.; Fitoussi, C.; Stracke, A. Chondritic Mg isotope composition of the Earth. *Geochim. Et Cosmochim. Acta* **2010**, *74*, 5069–5083. [CrossRef]
62. Liu, S.A.; Teng, F.Z.; He, Y.S.; Ke, S.; Li, S.G. Investigation of magnesium isotope fractionation during granite differentiation: Implication for Mg isotopic composition of the continental crust. *Earth Planet. Sci. Lett.* **2010**, *297*, 646–654. [CrossRef]
63. Li, W.Y.; Teng, F.Z.; Wing, B.A.; Xiao, Y.L. Limited magnesium isotope fractionation during metamorphic dehydration in metapelites from the Onawa contact aureole, Maine. *Geochem. Geophys. Geosystems* **2014**, *15*, 408–415. [CrossRef]
64. Wang, S.J.; Teng, F.Z.; Li, S.G.; Hong, J.A. Magnesium isotopic systematics of mafic rocks during continental subduction. *Geochim. Cosmochim. Acta* **2014**, *143*, 34–48. [CrossRef]
65. Wang, S.J.; Teng, F.Z.; Rudnick, R.J.; Li, S.G. The behavior of magnesium isotopes in low-grade metamorphosed mudrocks. *Geochim. Et Cosmochim. Acta* **2015**, *165*, 435–448. [CrossRef]
66. Dong, A.G.; Zhu, X.K.; Li, Z.H.; Kendall, B.; Li, S.Z.; Wang, Y.; Tang, C. A multi-isotope approach towards constraining the origin of large-scale Paleoproterozoic B-(Fe) mineralization in NE China. *Precambrian Res.* **2017**, *292*, 115–129. [CrossRef]
67. Chakrabarti, R.; Jacobsen, S.B. The isotopic composition of magnesium in the inner Solar System. *Earth Planet. Sci. Lett.* **2010**, *293*, 349–358. [CrossRef]
68. Handler, M.R.; Baker, J.A.; Schiller, M.; Bennett, V.C.; Yaxley, G.M. Magnesium stable isotope composition of Earth's upper mantle. *Earth Planet. Sci. Lett.* **2009**, *282*, 306–313. [CrossRef]

69. Huang, F.; Zhang, Z.F.; Lundstrom, C.C.; Zhi, X.C. Iron and magnesium isotopic compositions of peridotite xenoliths from Eastern China. *Geochim. Et Cosmochim. Acta* **2011**, *75*, 3318–3334. [CrossRef]
70. Young, E.D.; Galy, A. The isotope geochemistry and cosmochemistry of magnesium. *Rev. Mineral. Geochem.* **2004**, *55*, 197–230. [CrossRef]
71. Hippler, D.; Buhl, D.; Witbaard, R.; Richter, D.K.; Immenhauser, A. Towards a better understanding o magnesium-isotope ratios from marine skeletal carbonates. *Geochim. Cosmochim. Acta* **2009**, *73*, 6134–6146. [CrossRef]
72. Schauble, E.A. First-principles estimates of equilibrium magnesium isotope fractionation in silicate, oxide, carbonate and hexaaquamagnesium ($^{2+}$) crystals. *Geochim. Cosmochim. Acta* **2011**, *75*, 844–869. [CrossRef]
73. Teng, F.Z. Magnesium isotope geochemistry. *Rev. Mineral. Geochem.* **2017**, *82*, 219–287. [CrossRef]
74. Chaussidon, M.; Jambon, A. Boron content and isotopic composition of oceanic basalts: Geochemical and cosmochemical implications. *Earth Planet. Sci. Lett.* **1994**, *121*, 277–291. [CrossRef]
75. Swihart, G.H.; Moore, P.B.; Callis, E.L. Boron isotopic composition of marine and nonmarine evaporite borates. *Geochim. Et Cosmochim. Acta* **1986**, *50*, 1297–1301. [CrossRef]
76. Swihart, G.H.; Moore, P.B. A reconnaissance of the boron isotopic composition of tourmaline. *Geochim. Et Cosmochim. Acta* **1989**, *53*, 911–916. [CrossRef]
77. Palmer, M.R.; Slack, J.F. Boron isotopic composition of tourmaline from massive sulfide deposits and tourmalinites. *Contrib. Mineral. Petrol.* **1989**, *103*, 434–451. [CrossRef]
78. Palmer, M.R. Boron isotope systematics of hydrothermal fluids and tourmalines: A synthesis. *Chem. Geol.* **1991**, *94*, 111–121. [CrossRef]
79. Barth, S. Boron isotope variations in nature: A synthesis. *Geol. Rundsch.* **1993**, *82*, 640–651. [CrossRef]
80. Marschall, H.R.; Jiang, S.Y. Tourmaline isotopes: No element left behind. *Elements* **2011**, *7*, 313–319. [CrossRef]
81. Bast, R.; Scherer, E.E.; Mezger, K.; Austrheim, H.; Ludwig, T.; Marschall, H.R.; Putnis, A.; Löwen, K. Boron isotopes in tourmaline as a tracer of metasomatic processes in the Bamble sector of Southern Norway. *Contrib. Mineral. Petrol.* **2014**, *168*, 1069. [CrossRef]
82. Ishikawa, T.; Nakamura, E. Boron isotope systematics of marine sediments. *Earth Planet. Sci. Lett.* **1993**, *117*, 567–580. [CrossRef]
83. Palmer, M.R.; London, D.; Morgan, G.B.; Babb, H.A. Experimental determination of fractionation of $^{11}B/^{10}B$ between tourmaline and aqueous vapor: A temperature- and pressure-dependent isotopic system. *Chem. Geol.* **1992**, *101*, 123–129.
84. Palmer, M.R.; Swihart, G.H. Boron isotope geochemistry: An overview. In *Boron: Mineralogy, Petrology and Geochemistry*, 2nd ed.; Grew, E.S., Anovitz, I.M., Eds.; Mineralogical Society of America: Washington, DC, USA, 2002; pp. 709–744.
85. Marschall, H.R.; Ludwig, T.; Altherr, R.; Kalt, A.; Tonarini, S. Syros metasomatic tourmaline: Evidence for very high-$\delta^{11}B$ fluids in subduction zones. *J. Petrol.* **2006**, *47*, 1915–1942. [CrossRef]
86. Henry, D.J.; Guidotti, C.V. Tourmaline as a petrogenetic indicator mineral: An example from the staurolite-grade metapelites of NW Maine. *Am. Mineral.* **1985**, *70*, 1–15.
87. Slack, J.F.; Palmer, M.R.; Stevens, B.P.J.; Barnes, R.G. Origin and significance of tourmaline-rich rocks in the Broken Hill District, Australia. *Econ. Geol.* **1993**, *88*, 505–541. [CrossRef]
88. Jiang, S.Y. Boron isotope geochemistry of hydrothermal ore deposits in China: A preliminary study. *Phys. Chem. Earth* **2001**, *26*, 851–858. [CrossRef]
89. Marschall, H.R.; Altherr, R.; Kalt, A.; Ludwig, T. Detrital, metamorphic and metasomatic tourmaline in high-pressure metasediments from Syros (Greece): Intra-grain boron isotope patterns determined by secondary-ion mass spectrometry. *Contrib. Mineral. Petrol.* **2008**, *155*, 703–717. [CrossRef]
90. Chaussidon, M.; Albarède, F. Secular boron isotope variations in the continental crust: An ion microprobe study. *Earth Planet. Sci. Lett.* **1992**, *108*, 229–241. [CrossRef]
91. Zhai, M.G.; Santosh, M. Metallogeny of the North China Craton: Link with secular changes in the evolving Earth. *Gondwana Res.* **2013**, *24*, 275–297. [CrossRef]
92. Zhao, G.C.; Sun, M.; Wilde, S.A.; Li, S.Z. Late Archean to Paleoproterozoic evolution of the North China Craton: Key issues revisited. *Precambrian Res.* **2005**, *136*, 177–202. [CrossRef]
93. Zhai, M.G.; Santosh, M. The early Precambrian odyssey of the North China Craton: A synoptic overview. *Gondwana Res.* **2011**, *20*, 6–25. [CrossRef]

94. Zhao, G.C.; Cawood, P.A.; Li, S.Z.; Wilde, S.A.; Sun, M.; Zhang, J.; He, Y.H.; Yin, C.Q. Amalgamation of the North China Craton: Key issues and discussion. *Precambrian Res.* **2012**, *222*, 55–76. [CrossRef]
95. Diwu, C.R.; Sun, Y.; Zhao, Y.; Lai, S.C. Early Paleoproterozoic (2.45-2.20 Ga) magmatic activity during the period of global magmatic shutdown: Implications for the crustal evolution of the southern North China Craton. *Precambrian Res.* **2014**, *255*, 627–640. [CrossRef]
96. Kröner, A.; Compston, W.; Zhang, G.W.; Guo, A.L.; Todt, W. Age and tectonic setting of Late Archean greenstone-gneiss terrain in Henan Province, China, as revealed by single-grain zircon dating. *Geology* **1988**, *16*, 211–215. [CrossRef]
97. Liu, D.Y.; Wilde, S.A.; Wan, Y.S.; Wang, S.Y.; Valley, J.W.; Kita, N.; Dong, C.Y.; Xie, H.Q.; Yang, C.X.; Zhang, Y.X.; et al. Combined U-Pb, hafnium and oxygen isotope analysis of zircons from meta-igneous rocks in the southern North China Craton reveal multiple events in the Late Mesoarchean-Early Neoarchean. *Chem. Geol.* **2009**, *260*, 140–154. [CrossRef]
98. Wan, Y.S.; Wilde, S.A.; Liu, D.Y.; Yang, C.X.; Song, B.; Yin, X.Y. Further evidence for ~1.85 Ga metamorphism in the Central Zone of the North China Craton: SHRIMP U-Pb dating of zircon from metamorphic rocks in the Lushan area, Henan Province. *Gondwana Res.* **2006**, *9*, 189–197. [CrossRef]
99. Diwu, C.R.; Sun, Y.; Lin, C.L.; Wang, H.L. LA-(MC)-ICPMS U-Pb zircon geochronology and Lu-Hf isotope compositions of the Taihua complex in the southern margin of the North China Craton. *Chin. Sci. Bull.* **2010**, *55*, 2557–2571. [CrossRef]
100. Jia, X.L.; Zhu, X.Y.; Zhai, M.G.; Zhao, Y.; Zhang, H.; Wu, J.L.; Liu, T. Late Mesoarchean crust growth event: Evidence from the ca. 2.8 Ga granodioritic gneisses of the Xiaoqinling area, southern North China Craton. *Sci. Bull.* **2016**, *61*, 974–990. [CrossRef]
101. Zhang, G.W.; Bai, Y.B.; Sun, Y.; Guo, A.L.; Zhou, D.W.; Li, T.H. Composition and evolution of the Archaean crust in central Henan, China. *Precambrian Res.* **1985**, *27*, 7–35. [CrossRef]
102. Lu, J.S.; Zhai, M.G.; Lu, L.S.; Wang, H.Y.C.; Chen, H.X.; Peng, T.; Wu, C.M.; Zhao, T.P. Metamorphic *P-T-t* path retrieved from metapelites in the southeastern Taihua metamorphic complex, and the Paleoproterozoic tectonic evolution of the southern North China Craton. *J. Asian Earth Sci.* **2017**, *134*, 352–364. [CrossRef]
103. Chen, H.X.; Wang, J.; Wang, H.; Wang, G.D.; Peng, T.; Shi, Y.H.; Zhang, Q.; Wu, C.M. Metamorphism and geochronology of the Luoning metamorphic terrane, southern terminal of the Palaeoproterozoic Trans-North China Orogen, North China Craton. *Precambrian Res.* **2015**, *264*, 156–178. [CrossRef]
104. Zhao, T.P.; Zhai, M.G.; Xia, B.; Li, H.M.; Zhang, Y.X.; Wan, Y.S. Zircon U-Pb SHRIMP dating for the volcanic rocks of the Xiong'er Group: Constrains on the initial formation age of the cover of the North China Craton. *Chin. Sci. Bull.* **2004**, *49*, 2495–2502. [CrossRef]
105. Cui, M.L.; Zhang, B.L.; Peng, P.; Zhang, L.C.; Shen, X.L.; Guo, Z.H.; Huang, X.F. Zirocn/baddeleyite U-Pb dating for the Paleo-proterozoic intermediate-acid intrusion rocks in Xiaoshan Mountains, west of Henan Province and their constraints on the age of the Xiong'er Volcanic Province. *Acta Petrol. Sin.* **2010**, *26*, 1541–1549, (In Chinese with English Abstract).
106. Lu, J.S.; Wang, G.D.; Wang, H.; Chen, H.X.; Wu, C.M. Palaeoproterozoic metamorphic evolution and geochronology of the Wugang block, southeastern terminal of the Trans-North China. *Precambrian Res.* **2014**, *251*, 197–211. [CrossRef]
107. Yu, S.Y.; Li, S.Z.; Liu, K.J.; Zhuang, L.C.; Li, Z.C. A preliminary study on the mineralogy of the Zhaoanzhuang-type iron ore deposit, Wuyang, Henan Province. *Bull. Yichang Inst. Geol. Miner. Resour. Chin. Acad. Geol. Sci.* **1982**, *5*, 1–22, (In Chinese with English Abstract).
108. Li, Y.F.; Xie, K.J.; Luo, Z.Z.; Li, J.P. Geochemistry of Tieshan iron deposiy in the Wuyang area, Henan Province and its environment implications. *Acta Geol. Sin.* **2013**, *87*, 1377–1398, (In Chinese with English Abstract).
109. Su, B.X.; Teng, F.Z.; Hu, Y.; Shi, R.D.; Zhou, M.F.; Zhu, B.; Liu, F.; Gong, X.H.; Huang, Q.S.; Xiao, Y.; et al. Iron and magnesium isotope fractionation in oceanic lithosphere and sub-arc mantle: Perspectives from ophiolites. *Earth Planet. Sci. Lett.* **2015**, *430*, 523–532. [CrossRef]
110. Ding, T.P.; Li, H.; Zhang, G.B.; Li, Y.H.; Li, J.C. A study on determining $^{33}S/^{32}S$, $^{34}S/^{32}S$ and $^{36}S/^{32}S$ by SF_6 method. *Miner. Depos.* **1987**, *6*, 81–93, (In Chinese with English Abstract).
111. Hou, K.J.; Li, Y.H.; Wan, D.F. Constraints on the Archean atmospheric oxygen and sulfur cycle from mass-independent sulfur records from Anshan-Benxi BIFs, Liaoning Province, China. *Sci. China Ser. D Earth Sci.* **2007**, *50*, 1471–1478. [CrossRef]

112. Ke, S.; Teng, F.Z.; Li, S.G.; Gao, T.; Liu, S.A.; He, Y.S.; Mo, X.X. Mg, Sr and O isotope geochemistry of syenites from northwest Xinjiang, China: Tracing carbonate recycling during Tethyan oceanic subduction. *Chem. Geol.* **2016**, *437*, 109–119. [CrossRef]
113. Galy, A.; Yoffe, O.; Janney, P.E.; Williams, R.W.; Cloquet, C.; Alard, O.; Halicz, L.; Wadhwa, M.; Hutcheon, I.D.; Ramon, E.; et al. Magnesium isotope heterogeneity of the isotopic standard SRM980 and new reference materials for magnesium-isotope-ratio measurements. *J. Anal. At. Spectrom.* **2003**, *18*, 1352–1356. [CrossRef]
114. Teng, F.Z.; Li, W.Y.; Ke, S.; Yang, W.; Liu, S.A.; Sedaghatpour, F.; Wang, S.J.; Huang, K.J.; Hu, Y.; Ling, M.X.; et al. Magnesium isotopic compositions of international geological reference materials. *Geostand. Geoanalytical Res.* **2015**, *39*, 329–339. [CrossRef]
115. Hou, K.J.; Li, Y.H.; Xiao, Y.K.; Liu, F.; Tian, Y.R. In situ boron isotope measurements of natural geological materials by LA-MC-ICP-MS. *Chin. Sci. Bull.* **2010**, *55*, 3305–3311. [CrossRef]
116. Brown, J.S. Sulfur isotopes of Precambrian sulfates and sulfides in the Grenville of New York and Ontario. *Econ. Geol.* **1973**, *68*, 362–370. [CrossRef]
117. Chu, X.L.; Chen, J.S.; Wang, S.X. Study on fractionation mechanism of sulfur isotope and physicochemical conditions of alteration and ore formation in Luohe iron deposit, Anhui. *Sci. Geol. Sin.* **1986**, *3*, 276–289, (In Chinese with English Abstract).
118. Palmer, M.R.; Helvací, C.; Fallick, A.E. Sulfur, sulphate oxygen and strontium isotope composition of Cenozoic Turkish evaporites. *Chem. Geol.* **2004**, *209*, 341–356. [CrossRef]
119. Geske, A.; Goldstein, R.H.; Mavromatis, V.; Richter, D.K.; Buhl, D.; Kluge, T.; John, C.M.; Immenhauser, A. The magnesium isotope (δ^{26}Mg) signature of dolomites. *Geochim. Cosmochim. Acta* **2015**, *149*, 131–151. [CrossRef]
120. Huang, K.J.; Shen, B.; Lang, X.G.; Tang, W.B.; Peng, Y.; Ke, S.; Kaufman, A.J.; Ma, H.R.; Li, F.B. Magnesium isotopic compositions of the Mesoproterozoic dolostones: Implications for Mg isotopic systematics of marine carbonates. *Geochim. Cosmochim. Acta* **2015**, *164*, 333–351. [CrossRef]
121. Li, F.B.; Teng, F.Z.; Chen, J.T.; Huang, K.J.; Wang, S.J.; Lang, X.G.; Ma, H.R.; Peng, Y.B.; Shen, B. Constraining ribbon rock dolomitization by Mg isotopes: Implications for the 'dolomite problem'. *Chem. Geol.* **2016**, *445*, 208–220. [CrossRef]
122. Seal, R.R.; Alpers, C.N.; Rye, R.O. Stable isotope systematics of sulfate minerals. In *Sulfate Minerals—Crystallography: Geochemistry and Environment Significance*; Alpers, C.N., Jamber, J.L., Nordstrom, D.K., Eds.; Mineral Society of America: Chantill, VA, USA, 2000; pp. 541–602.
123. Böttcher, M.E.; Schale, H.; Schnetger, B.; Wallmann, K.; Brumsack, H.-J. Stable sulfur isotopes indicate net sulfate reduction in near-surface sediments of the deep Arabian Sea. *Deep-Sea Res. Ii* **2000**, *47*, 2769–2783.
124. Böttcher, M.E.; Brumsack, H.-J.; Dürselen, C.-D. The isotopic composition of modern seawater sulfate: I. Coastal waters with special regard to the North Sea. *J. Mar. Syst.* **2007**, *67*, 73–82. [CrossRef]
125. Li, Y.H.; Duan, C.; Han, D.; Chen, X.W.; Wang, C.L.; Yang, B.Y.; Zhang, C.; Liu, F. Effect of sulfate evaporate salt layer for formation of porphyrite iron ores in the Middle-Lower Yangtze River area. *Acta Petrol. Sin.* **2014**, *30*, 1355–1368, (In Chinese with English Abstract).
126. Barth, A.P.; Dorais, M.J. Magmatic anhydrite in granitic rocks: First occurrence and potential petrologic onsequences. *Am. Mineral.* **2000**, *85*, 430–435. [CrossRef]
127. Swanson, S.E.; Kearney, C.S. Anhydrite in the 1989-1990 lavas and xenoliths from Redoubt Volcano, Alaska. *J. Volcanol. Geotherm. Res.* **2008**, *175*, 509–516. [CrossRef]
128. Farquhar, J.; Savarino, J.; Airieau, S.; Thiemens, M.H. Observation of wavelength-sensitive mass-independent sulfur isotope effects during SO_2 photolysis: Implications for the early atmosphere. *J. Geophys. Res.* **2001**, *106*, 32829–32839. [CrossRef]
129. Penniston-Dorland, S.C.; Mathez, E.A.; Wing, B.A.; Farquhar, J.; Kinnaird, J.A. Multiple sulfur isotope evidence for surface-derived sulfur in the Bushveld Complex. *Earth Planet. Sci. Lett.* **2012**, *337–338*, 236–242. [CrossRef]
130. Farquhar, J.; Wing, B.A. Multiple sulfur isotopes and the evolution of the atmosphere. *Earth Planet. Sci. Lett.* **2003**, *213*, 1–13. [CrossRef]
131. Hu, G.X.; Rumble, D.; Wang, P.L. An ultraviolet laser microprobe for the in situ analysis of multisulfur isotopes and its use in measuring Archean sulfur isotope mass-independent anomalies. *Geochim. Cosmochim. Acta* **2003**, *67*, 3101–3117. [CrossRef]

132. Ono, S.H.; Kaufman, A.J.; Farquhar, J.; Sumner, D.Y.; Beukes, N.J. Lithofacies control on multiple-sulfur isotope records and Neoarchean sulfur cycles. *Precambrian Res.* **2009**, *169*, 58–67. [CrossRef]
133. Paris, G.; Adkins, J.F.; Sessions, A.L.; Webb, S.M.; Fischer, W.W. Neoarchean carbonate-associated sulfate records positive $\Delta^{33}S$ anomalies. *Science* **2014**, *346*, 739–741. [CrossRef] [PubMed]
134. Ono, S.H.; Beukes, N.J.; Rumble, D. Origin of two distinct multiple-sulfur isotope compositions of pyrite in the 2.5 Ga Klein Naute Formation, Griqualand West Basin, South Africa. *Precambrian Res.* **2009**, *169*, 48–57. [CrossRef]
135. Li, Y.H.; Hou, K.J.; Wan, D.F.; Zhang, Z.J.; Yue, G.L. Formation mechamism of Precambrian banded iron formation and atmosphere and ocean during early stage of the Earth. *Acta Geol. Sin.* **2010**, *84*, 1359–1373, (In Chinese with English Abstract).
136. Gross, G.A. A classification of iron-formation based on depositional environments. *Can. Mineral.* **1980**, *18*, 215–222.
137. Wen, G.; Bi, S.J.; Li, J.W. Role of evaporitic sulfates in iron skarn mineralization: A fluid inclusion and sulfur isotope study from the Xishimen deposit, Handan-Xingtai district, North China Craton. *Miner. Depos.* **2017**, *52*, 495–514. [CrossRef]
138. Li, Y.H.; Xie, G.Q.; Duan, C.; Han, D.; Wang, C.L. Effect of sulfate evaporate salt layer over the formation of skarn-type iron ore. *Acta Geol. Sin.* **2013**, *87*, 1324–1334, (In Chinese with English Abstract).
139. Ling, M.X.; Sedaghatpour, F.; Teng, F.Z.; Hays, P.D.; Strauss, J.; Sun, W.D. Homogenous magnesium isotopic composition of seawater: An excellent geostandard for Mg isotope analysis. *Rapid Commun. Mass Spectrom.* **2011**, *25*, 2828–2836. [CrossRef]
140. Wang, S.J.; Teng, F.Z.; Li, S.G.; Hong, J.A. Tracing carbonate-silicate interaction during subduction using magnesium and oxygen isotopes. *Nat. Commun.* **2014**, *5*, 5328. [CrossRef] [PubMed]
141. Zhao, X.M.; Cao, H.H.; Mi, Y.; Evans, N.J.; Qi, Y.H.; Huang, F.; Zhang, H.F. Combined iron and magnesium isotope geochemistry of pyroxenite xenoliths from Hannuoba, North China Craton: Implications for mantle metasomatism. *Contrib. Mineral. Petrol.* **2017**, *172*, 40. [CrossRef]
142. Li, S.G.; Yang, W.; Ke, S.; Meng, X.N.; Tian, H.C.; Xu, L.J.; He, Y.S.; Huang, J.; Wang, X.C.; Xia, Q.K.; et al. Deep carbon cycles constrained by a large-scale mantle Mg isotope anomaly in eastern China. *Natl. Sci. Rev.* **2017**, *4*, 111–120. [CrossRef]
143. Li, W.Y.; Teng, F.Z.; Halama, R.; Keller, J.; Klaudius, J. Magnesium isotope fractionation during carbonatite magmatism at Oldoinyo Lengai, Tanzania. *Earth Planet. Sci. Lett.* **2016**, *444*, 26–33. [CrossRef]
144. Foster, G.L.; Pogge von Strandmann, P.A.E.; Rae, J.W.B. Boron and magnesium isotopic composition of seawater. *Geochem. Geophys. Geosystems* **2010**, *11*, 1–10. [CrossRef]
145. Dong, A.G.; Zhu, X.K.; Li, S.Z.; Kendall, B.; Wang, Y.; Gao, Z.F. Genesis of a giant Paleoproterozoic strata-bound magnesite deposit: Constraints from Mg isotopes. *Precambrian Res.* **2016**, *281*, 673–683. [CrossRef]
146. Shen, B.; Wimpenny, J.; Lee, C.T.A.; Tollstrup, D.; Yin, Q.Z. Magnesium isotope systematics of endoskarns: Implications for wallrock reaction in magma chambers. *Chem. Geol.* **2013**, *356*, 209–214. [CrossRef]
147. Chen, C.X.; Lu, A.H.; Cai, K.Q.; Zhai, Y.S. Sedimentary characteristics of Mg-rich carbonate formations and minerogenic fluids of magnesite and talc occurrences in early Proterozoic in eastern Liaoning Province, China. *Sci. China (Ser. B)* **2002**, *45*, 84–92. [CrossRef]
148. Chaussidon, M.; Marty, B. Primitive boron isotope composition of the mantle. *Science* **1995**, *269*, 383–386. [CrossRef]
149. Marschall, H.R.; Dorsey Wanless, V.; Shimizu, N.; Pogge von Strandmann, P.A.E.; Elliott, T.; Monteleone, B.D. The boron and lithium isotopic composition of mid-ocean ridge basalts and the mantle. *Geochim. Cosmochim. Acta* **2017**, *207*, 102–138. [CrossRef]
150. Vengosh, A.; Starinsky, A.; Kolodny, Y.; Chivas, A.R.; Raab, M. Boron isotope variations during fractional evaporation of seawater: New constraints on the marine vs. nonmarine debate. *Geology* **1992**, *20*, 799–802. [CrossRef]
151. Byerly, G.R.; Palmer, M.R. Tourmaline mineralization in the Barberton greenstone belt, South Africa: Early Archean metasomatism by evaporate-derived boron. *Contrib. Mineral. Petrol.* **1991**, *107*, 387–402. [CrossRef] [PubMed]
152. Trumbull, R.B.; Beurlen, H.; Wiedenbeck, M.; Soares, D.R. The diversity of B-isotope variations in tourmaline from rare-element pegmatites in the Borborema Province of Brazil. *Chem. Geol.* **2013**, *352*, 47–62. [CrossRef]

153. Jiang, S.Y.; Palmer, M.R. Boron isotope systematics of tourmaline from granites and pegmatites: A synthesis. *Eur. J. Mineral.* **1998**, *10*, 1253–1265. [CrossRef]
154. Slack, J.F.; Palmer, M.R.; Stevens, B.P.J. Boron isotope evidence for the involvement of non-marine evaporates in the origin of the Broken Hill ore deposits. *Nature* **1989**, *342*, 913–916. [CrossRef]
155. Peng, Q.M.; Palmer, M.R. The Paleoproterozoic borate deposits in eastern Liaoning, China: A metamorphosed evaporate. *Precambrian Res.* **1995**, *72*, 185–197. [CrossRef]
156. Yan, X.L.; Chen, B. Chemical and boron isotopic compositions of tourmaline from the Paleoproterozoic Houxianyu borate deposit, NE China: Implications for the origin of borate deposit. *J. Asian Earth Sci.* **2014**, *94*, 252–266. [CrossRef]
157. Van Hinsberg, V.J.; Schumacher, J.C. Tourmaline as a petrogenetic indicator mineral in the Haut-Allier metamorphic suite, massif central, France. *Can. Mineral.* **2011**, *49*, 177–194. [CrossRef]
158. Meyer, C.; Wunder, B.; Meixner, A.; Romer, R.L.; Heinrich, W. Boron-isotope fractionation between tourmaline and fluid: An experimental re-investigation. *Contrib. Mineral. Petrol.* **2008**, *156*, 259–267. [CrossRef]
159. Zhang, X.Q.; Song, X.Y.; Chen, L.M.; Xie, W.; Yu, S.Y.; Zheng, W.Q.; Deng, Y.F.; Zhang, J.F.; Gui, S.G. Fractional crystallization and the formation of thick Fe-Ti-V oxide layers in the Baima layered intrusion, SW China. *Ore Geol. Rev.* **2012**, *49*, 96–108. [CrossRef]
160. Liu, P.P.; Zhou, M.F.; Chen, W.T.; Boone, M.; Cnudde, V. Using multiphase solid inclusions to constrain the origin of the Baima Fe-Ti-(V) oxide deposit, SW China. *J. Petrol.* **2014**, *55*, 951–976. [CrossRef]
161. Liu, P.P.; Zhou, M.F.; Ren, Z.Y.; Wang, C.Y.; Wang, K. Immiscible Fe- and Si-rich silicate melts in plagioclase from the Baima mafic intrusion (SW China): Implications for the origin of bi-modal igneous suites in large igneous provinces. *J. Asian Earth Sci.* **2016**, *127*, 211–230. [CrossRef]
162. Wang, C.Y.; Zhou, M.F.; Zhao, D.G. Fe-Ti-Cr oxides from the Permian Xinjie mafic-ultramafic layered intrusion in the Emeishan large igneous province, SW China: Crystallization from Fe- and Ti-rich basaltic magmas. *Lithos* **2008**, *102*, 198–217. [CrossRef]
163. Pang, K.N.; Li, C.; Zhou, M.F.; Ripley, E.M. Mineral compositional constraints on petrogenesis and oxide ore genesis of the late Permian Panzhihua layered gabbroic intrusion, SW China. *Lithos* **2009**, *110*, 199–214. [CrossRef]
164. Bai, Z.J.; Zhong, H.; Naldrett, A.J.; Zhu, W.G.; Xu, G.W. Whole-rock and mineral composition constraints on the genesis of the giant Hongge Fe-Ti-V oxide deposit in the Emeishan Large Igneous Province, Southwest China. *Econ. Geol.* **2012**, *107*, 507–524. [CrossRef]
165. Bai, Z.J.; Zhong, H.; Li, C.; Zhu, W.G.; He, D.F.; Qi, L. Contrasting parental magma compositions for the Hongge and Panzhihua magmatic Fe-Ti-V oxide deposits, Emeishan Large Igneous Province, SW China. *Econ. Geol.* **2014**, *109*, 1763–1785. [CrossRef]
166. Zhang, Z.C.; Mahoney, J.J.; Mao, J.W.; Wang, F.S. Geochemistry of picritic and associated basalt flows of the Western Emeishan flood basalt province, China. *J. Petrol.* **2006**, *47*, 1997–2019. [CrossRef]
167. Zhang, Z.C.; Mahoney, J.J.; Wang, F.S.; Zhao, L.; Ai, Y.; Yang, T.Z. Geochemistry of picritic and associated basalt flows of the western Emeishan flood basalt province, China: Evidence for a plume-head origin. *Acta Petrol. Sin.* **2006**, *22*, 1538–1552, (In Chinese with English Abstract).
168. Zhang, Z.C.; Li, Y.; Zhao, L.; Ai, Y. Geochemistry of three layered mafic-ultramafic intrusions in the Panxi area and constraints on their sources. *Acta Petrol. Sin.* **2007**, *23*, 2339–2352, (In Chinese with English Abstract).
169. Song, X.Y.; Qi, H.W.; Hu, R.Z.; Chen, L.M.; Yu, S.Y.; Zhang, J.F. Formation of thick stratiform Fe-Ti oxide layers in layered intrusion and frequent replenishment of fractionated mafic magma: Evidence from the Panzhihua intrusion, SW China. *Geochem. Geophys. Geosystems* **2013**, *14*, 712–732. [CrossRef]
170. Yu, M.; Feng, C.Y.; Bao, G.Y.; Liu, H.C.; Zhao, Y.M.; Li, D.X.; Xiao, Y.; Liu, J.N. Characteristics and zonation of skarn minerals in Galinge iron deposit, Qinghai Province. *Miner. Depos.* **2013**, *32*, 55–76, (In Chinese with English Abstract).
171. Lee, C.H.; Lee, H.K.; Kim, S.J. Geochemistry and mineralization age of magnesian skarn-type iron deposits of the Janggun mine, Republic of Korea. *Miner. Depos.* **1998**, *33*, 379–390. [CrossRef]
172. Huang, X.W.; Gao, J.F.; Qi, L.; Zhou, M.F. In-situ LA-ICP-MS trace element analyses of magnetite and Re-Os dating of pyrite: The Tianhu hydrothermally remobilized sedimentary Fe deposit, NW China. *Ore Geol. Rev.* **2015**, *65*, 900–916. [CrossRef]

173. Zheng, J.H.; Mao, J.W.; Yang, F.Q.; Chai, F.M.; Shen, P. Petrological and geochemical features of the early Paleozoic granitic gneisses and iron ores in the Tianhu iron deposit, Eastern Tianshan NW China: Implications for ore genesis. *Lithos* **2017**, *286–297*, 426–439. [CrossRef]
174. Sun, Y.B. Geological characteristics and metallogenic types of the Lilaozhuang iron-magnesite deposit in Huoqiu, Anhui. *Miner. Resour. Geol.* **2007**, *21*, 532–537, (In Chinese with English Abstract).
175. Huang, H.; Zhang, L.C.; Liu, X.F.; Li, H.Z.; Liu, L. Geological and geochemical characteristics of the Lee Laozhuang iron mine in Huoqiu iron deposit: Implications for sedimentary environment. *Acta Petrol. Sin.* **2013**, *29*, 2593–2605, (In Chinese with English Abstract).
176. Huang, H.; Zhang, L.C.; Fabre, S.; Wang, C.L. Depositional environment and origin of the Lilaozhuang Neoarchean BIF-hosted iron-magnesite deposit on the southern margin of the North China Craton. *Int. J. Earth Sci.* **2017**, *106*, 1753–1772. [CrossRef]
177. Yang, X.Y.; Liu, L.; Lee, I.; Wang, B.H.; Du, Z.B.; Wang, Q.C.; Wang, Y.X.; Sun, W.D. A review on the Huoqiu banded iron formations (BIF), southeast margin of the North China Craton: Genesis of iron deposits and implications for exploration. *Ore Geol. Rev.* **2014**, *63*, 418–443. [CrossRef]
178. Peng, Q.M.; Palmer, M.R. The Paleoproterozoic Mg and Mg-Fe borate deposits of Liaoning and Jilin Provinces, Northeast China. *Econ. Geol.* **2002**, *97*, 93–108. [CrossRef]
179. Hu, G.Y.; Fan, C.F.; Li, Y.H.; Hou, K.J.; Liu, Y.; Chen, X. Marine evaporative genesis of Mg-borate deposits in the Zhuanmiao ore district, Eastern Liaoning Province: Evidence from B, S, C isotopes. *Acta Geosci. Sin.* **2014**, *35*, 445–453, (In Chinese with English Abstract).
180. Meinert, L.D. Skarns and skarn deposits. *Geosci. Can.* **1992**, *19*, 145–162.
181. Yu, M.; Feng, C.Y.; Zhu, Z.F.; Mao, J.W.; Zhao, Y.M.; Li, D.X. Multistage amphiboles from the Galinge iron skarn deposit in Qiman Tagh, western China: Evidence of igneous rocks replacement. *Mineral. Petrol.* **2017**, *111*, 81–97. [CrossRef]
182. Pons, J.M.; Franchini, M.; Meinert, L.; Recio, C.; Etcheverry, R. Iron skarns of the Vegas Peladas District, Mendoza, Argentina. *Econ. Geol.* **2009**, *104*, 157–184. [CrossRef]
183. Jiang, S.Y.; Palmer, M.R.; Peng, Q.M.; Yang, J.H. Chemical and stable isotopic compositions of Proterozoic metamorphosed evaporites and associated tourmalines from the Houxianyu borate deposit, eastern Liaoning, China. *Chem. Geol.* **1997**, *135*, 189–211. [CrossRef]
184. Hu, G.Y.; Li, Y.H.; Fan, C.F.; Hou, K.J.; Zhao, Y.; Zeng, L.S. In situ LA-MC-ICP-MS boron isotope and zircon U-Pb age determinations of Paleoproterozoic borate deposits in Liaoning Province, northeastern China. *Ore Geol. Rev.* **2015**, *65*, 1127–1141. [CrossRef]